Manuscript Details

Manuscript number	ENGEO_2020_429
Title	Effect of slit size on the impact load against debris-flow mitigation dams
Article type	Research Paper

Abstract

Structural countermeasures such as slit dams and check dams are widely installed in mountainous regions to mitigate debris-flow hazards. However, current approaches adopted to estimate debris-flow impact load only depend on the flow properties without considering the effect of structural geometry. To better understand the effect of slit size on the impact load against debris-flow mitigation dams, a series of debris flows impact tests on the modelled slit dams and check dams were conducted in an instrumented flume. A combination of the flow velocity, depth, impact loads, total basal normal stress, and basal pore-fluid pressure measurement enabled a comprehensive grasp of the impact details. Tests reveal that the peak frontal impact pressure is almost not affected by the slit size of structural countermeasures instead by the debris-flow properties. However, the slit size obviously influences the peak force experienced by the structures. A critical relative slit size (ratio of slit size to the maximum particle diameter in debris flow) 3.6 is determined for slit dam to effectively mitigate debris-flow hazards. In addition, a bilinear pressure distribution model is proposed for debris-flow impact load estimation of the slit dams and check dams.

Keywords	Debris-flow hazards; slit dam; slit size; check dam; impact load; physical model test.
Taxonomy	Geotechnics, Landslide, Engineering Geology, Geological Hazard

Corresponding Author	Gordon ZHOU
Corresponding Author's Institution	Chinese Academy of Sciences
Order of Authors	Hongsen Hu, Gordon ZHOU, Dongri Song, Kahlil Fredrick E. Cui, Yu Huang, Clarence Choi, Huayong Chen
Suggested reviewers	Johannes Hübl, Julian KWAN, Alessandro Leonardi

Submission Files Included in this PDF

File Name [File Type]

Cover letter.docx [Cover Letter]

Highlights.docx [Highlights]

Manuscript.docx [Manuscript File]

Figures.docx [Figure]

Tables.docx [Table]

Conflict of Interest.docx [Conflict of Interest]

Author Statement.docx [Author Statement]

To view all the submission files, including those not included in the PDF, click on the manuscript title on your EVISE Homepage, then click 'Download zip file'.

Research Data Related to this Submission

There are no linked research data sets for this submission. The following reason is given:
Data will be made available on request

Professor Hsein Juang, Dr. Vicki Moon, and Dr. Janusz Wasowski
Editors-in-Chief
Engineering Geology

Dear Prof. Juang, Dr. Vicki Moon, and Dr. Janusz Wasowski

Effect of slit size on the impact load against debris-flow mitigation dams

Hongsen Hu, Gordon G. D. Zhou, Dongri Song, Kahlil Fredrick E. Cui, Yu Huang, Clarence E. Choi, Huayong Chen

We would like to submit a manuscript entitled "Effect of slit size on the impact load against debris-flow mitigation dams" for review and possible publication in Engineering Geology.

In this manuscript, experiments show that the peak frontal pressure is largely unaffected by the slit size of countermeasure structures instead of by the incoming flow properties. However, when considering the contribution of the static component caused by the gravity to the impact load, the slit size make significant influence on the peak impact force exerted on the structures, which is regarded as the most critical design scenario. In addition, a critical relative slit size (ratio of slit size to the maximum particle diameter in debris flow) 3.6 is determined for slit dam to effectively mitigate debris-flow hazards. At last, bilinear pressure distribution models are proposed for debris-flow impact load estimation of the slit dams and check dams.

We believe the results can open the way for new, and more advanced, design prescriptions for debris-flow mitigation dams. The material in the manuscript is original and has not been published elsewhere.

The following documents have been enclosed for your consideration:
1. Highlights
2. Copy of the manuscript
3. File containing figures
4. File containing tables
5. Conflict of Interest
6. Author Statement

Should you have any concerns, please do not hesitate to contact me at gordon@imde.ac.cn.

Sincerely
Gordon G. D. Zhou
Institute of Mountain Hazards and Environment, Chinese Academy of Sciences

Highlights

- Peak frontal pressure is largely unaffected by the slit size of countermeasure structures.
- Slit size make significant influence on the peak impact force considering the contribution of the static component.
- Critical b/D_{max}=3.6 (b: slit size; D_{max}: the maximum particle diameter) is determined for slit dam to effectively mitigate debris-flow hazards.
- Bilinear pressure distribution models are proposed for debris-flow impact load estimation of the slit dams and check dams.

General information of the article

Type of paper: Article

Title: Effect of slit size on the impact load against debris-flow mitigation dams

Authors: Hongsen Hu[1&2], Gordon G. D. Zhou*[1&2], Dongri Song[1&2], Kahlil Fredrick E. Cui[1&2], Yu Huang[3], Clarence E. Choi[4], Huayong Chen[1&2]

1. Key Laboratory of Mountain Hazards and Earth Surface Process/Institute of Mountain Hazards and Environment, Chinese Academy of Sciences (CAS), Chengdu, China

2. University of Chinese Academy of Sciences, Beijing, China

3. Department of Geotechnical Engineering, College of Civil Engineering, Tongji University, Shanghai, China

4. Department of Civil Engineering, the University of Hong Kong, Hong Kong, China

*Corresponding author

Information of the authors

Corresponding author: Dr. Gordon G. D. Zhou
Professor
E-mail: gordon@imde.ac.cn

Co-author: Mr. H. S. Hu
Ph.D student
E-mail: huhongsen15@mails.ucas.edu.cn

Co-author: Dr. D. Song
Associate Professor
E-mail: drsong@imde.ac.cn

Co-author: Mr. Kahlil Fredrick E. Cui
Ph.D. Student
E-mail: kfcui@imde.ac.cn

Co-author: Dr. Yu Huang
Professor
E-mail: yhuang@tongji.edu.cn

Co-author: Dr. Clarence E. Choi
Assistant Professor
E-mail: cechoi@hku.hk

Co-author: Dr. Huayong Chen
Professor
E-mail: hychen@imde.ac.cn

Effect of slit size on the impact load against debris-flow mitigation dams

Abstract: Structural countermeasures such as slit dams and check dams are widely installed in mountainous regions to mitigate debris-flow hazards. However, current approaches adopted to estimate debris-flow impact load only depend on the flow properties without considering the effect of structural geometry. To better understand the effect of slit size on the impact load against debris-flow mitigation dams, a series of debris flows impact tests on the modelled slit dams and check dams were conducted in an instrumented flume. A combination of the flow velocity, depth, impact loads, total basal normal stress, and basal pore-fluid pressure measurement enabled a comprehensive grasp of the impact details. Tests reveal that the peak frontal impact pressure is almost not affected by the slit size of structural countermeasures instead by the debris-flow properties. However, the slit size obviously influences the peak force experienced by the structures. A critical relative slit size (ratio of slit size to the maximum particle diameter in debris flow) 3.6 is determined for slit dam to effectively mitigate debris-flow hazards. In addition, a bilinear pressure distribution model is proposed for debris-flow impact load estimation of the slit dams and check dams.

Keywords: Debris-flow hazards; slit dam; slit size; check dam; impact load; physical model test.

1. Introduction

Multiple types of debris-flow mitigation dams are commonly constructed along the predicted flow channels to mitigate hazardous debris flows (Baldwin et al. 1987; VanDine, 1996; Hübl et al. 2005; Chen et al., 2015; Wei et al., 2017; Kattel et al., 2018; Poudyal et al., 2019). This includes check dams (Jaeggi et al. 1997; Shen et al., 2018; Li et al., 2019; Chen et al., 2019) or rigid barriers (Song et al., 2017; Koo et al., 2017; Cui et al. 2018), slit structures (Lin et al., 2017; Xie et al., 2017; Choi et al., 2018; Leonardi, 2019a & 2019b), and flexible barriers (Wendeler et al., 2007; Ferrero et al., 2015; Huo et al., 2017; Song et al., 2019), etc. As shown in Fig. 1, damage to these countermeasures results from underestimating the impact loads of debris flows. In order to design safe and effective countermeasures, potential debris flow impact loads have to be accurately estimated (Gao et al., 2017).

In current engineering practice, the most commonly accepted continuum-loading model used to predict the debris-flow impact loads exerting on barriers is the hydro-dynamic model (Hungr et al., 1984; Hübl and Holzinger, 2003; Kwan 2012; Bugnion et al., 2012; Volkwein, 2014), which is given as follows:

$$F=\alpha\rho v^2 hw \tag{1}$$

where α is the empirical dynamic pressure coefficient used to account for complexity of uncertainties involved in unknown flow composition, barrier type, impact mechanisms, and natural settings (Song et al., 2017; Poudyal et al., 2019). ρ is bulk density (kg/m^3), v is frontal velocity (m/s), h is the maximum approaching flow depth

(m) (because the damage to structures usually happens when the debris flow is deepest), and w is barrier width (m). This continuum-loading model is deduced from the conservation of momentum, supposing that the peak impact force (F_{peak}) is generated upon frontal impact and is proportional to the dynamic pressure. The simplicity of the model makes it is convenient for engineers to design countermeasures. The empirical dynamic pressure coefficient (α) is commonly estimated from the measured peak impact pressure (P_{peak}) against obstacles normalized by the bulk density (ρ) and the square of frontal debris-flow velocity (v^2) from physical flume experiments or from monitoring of real debris flow events.

Previous works have proposed different values of α in equation (1). Hungr et al. (1984) used the hydro-dynamic formulation (in equation 2) to estimate the dynamic impact force of debris flows in British Columbia:

$$F_{peak}=1.5A\rho v^2 sin\beta \quad (2)$$

where A is the flow cross-section area (m^2), β is the lowest angle between the flow direction and the face of barrier (°). Based on the field study of debris flows in the coastal and interior regions of British Columbia, the α value of 1.5 is obtained which accounts for the formation of stagnant wedges at the toe of the barriers.

Through a series of small-scale flume experiments, Hübl and Holzinger (2003) found that α varies from 0.1 to 3.9 and is dependent on the Froude conditions of flows. Furthermore, they developed a scale-independent relationship to predict the peak impact pressure of debris flows:

$$P_{peak}=4.5\rho v^{0.8}(gh)^{0.6} \quad (3)$$

which can also be written as:

$$P_{peak}=(4.5Fr^{-1.2})\rho v^2 \quad (4)$$

where g is the gravitational acceleration (m/s^2). Fr is the Froude number which is used to quantify the ratio of inertial and gravitational forces：

$$Fr=\frac{v}{\sqrt{gh}} \quad (5)$$

In addition, the results from 27 sets of experiments conducted by Cui et al. (2015) revealed that α varies in the range of 0.4 to 2.0. Along with results from 155 small-scale experiments cited from literatures, they revised the hydro-dynamic formulation as follows:

$$P_{peak}=(5.3Fr^{-1.6})\rho v^2 \quad (6)$$

More details about the hydro-dynamic equation are summarized in Table 1.

Studies have demonstrated that different structure types, such as rigid barriers and flexible barriers, have significantly different response to debris flow impact (Canelli et al., 2012; Ng et al., 2016). Proske et al. (2011) reported that the interaction between debris flow and obstacle is related to the geometry of the structure. Thus, it can be inferred that the type of countermeasure structure and its corresponding features (*i.e.*, slit size) should also be considered when determining for the value of α. This study focuses on the influence of slit size (b) on the impact load which debris flows exert on mitigation dams. The normalized slit size by the maximum particle diameter D_{max} in the debris flow is called the relative slit size b/D_{max}. Force measurements will be also

compared with those exerted on check dam (*i.e.*, b =0, b/D_{max}=0). The impact pressure distribution of debris flows on both slit dams and check dams are also investigated, which includes the distribution characteristics of the impact pressure along the height of dams as a function of time, as well as the effect of b/D_{max} and solid fraction (C_s) on the impact load.

2. Methodology

Physical test data, which are used to study the interaction between mass movement and structural countermeasures can be obtained through field measurements, large-scale instrumented tests, and small-scale flume experiments. Field measurements are oftentimes unfeasible due to the unpredictability of natural debris-flow events, and are to some extent unreliable due to the uncertainties involved in the explanations of field debris flows (Hong et al., 2015). Large-scale instrumented tests, such as those conducted in the USGS large debris-flow flume, would be a good substitute but would require high operational costs (Major, 1997; Ng et al., 2016). Small-scale flume experiments, on the other hand, provide a systematic and controlled mean to investigate the mechanisms of flow-structure interaction (Choi et al., 2015; Zhou et al., 2019a), although the viscous effects may be quite significant at miniature scales and the dissipation of nonequilibrium pore water pressure occurs rapidly compared with those of natural debris flows (Iverson et al., 2004; 2015). Despite this, extensive small-scale flume experiments have been carried out to study debris flow impact on structural countermeasures (Choi et al., 2014; Ng et al., 2015; Ng et al., 2016; Zhou et al., 2019a).

2.1 *Scaling principles*

Scaling is a powerful tool which enables the design of small-scale physical experiments in such a way that the results obtained therein can be interpreted similarly as those obtained from large-scale experiments or natural events (Holsapple, 1993; Iverson, 1997a; Zhou and Ng, 2010). In this section, the use of dimensionless groups ensures that the ratios between the main stresses between fluid and particles in the physical model tests match those estimated in prototypes.

The *Fr* macroscopically governs the behavior of geophysical flows, whether debris flows are dominated by inertial or gravitational forces (Hübl et al., 2009; Choi et al., 2015). This key dimensionless parameter is widely used to scale debris flow interaction with structures (Hübl et al., 2009; Armanini et al., 2011). Equation 5 can be re-written as:

$$Fr = \frac{v}{\sqrt{ghcos\theta}} \tag{7}$$

to accommodate for the effect of bed surface inclination (Choi et al. 2015).

The mobility of debris flows is mesoscopically effected by the collisional, frictional, and viscous stresses (Iverson, 1997a; Parsons et al., 2015; Iverson and Denlinger, 2001; Haas et al., 2015; Zhou et al., 2019b). In this study, the ratio of collisional to viscous stress is characterized by the Bagnold number N_{Bag}:

$$N_{\mathrm{Bag}} = \frac{C_s \rho_s d_{50}^2 \dot{\gamma}}{(1 - C_s)\mu} \tag{8}$$

The Savage number N_{Sav} (Savage, 1984; Savage and Hutter, 1989):

$$N_{\mathrm{Sav}} = \frac{\rho_s d_{50}^2 \dot{\gamma}^2}{(\rho_s - \rho_f) g h tan\varphi} \quad (9)$$

is used to characterize the ratio of stresses from grain collision and contact friction at the mesoscopic scale.

The relative dominance between the grain contact friction and the fluid viscous stress is characterized by the Friction number N_{Fric}:

$$N_{\mathrm{Fric}} = \frac{C_s(\rho_s - \rho_f) g h tan\varphi}{(1 - C_s)\dot{\gamma}\mu} \quad (10)$$

In equations (8)-(10), the C_s is volumetric solid fraction, ρ_s is bulk density of solid grains (kg/m^3), and d_{50} is median size of solid grains (m). The $\dot{\gamma}$ is shear rate of debris flow (1/s), which is approximated as the ratio of flow velocity and flow depth (*i.e.*, $\dot{\gamma} = v/h$). μ is dynamic viscosity of pore fluid (Pa.s), ρ_f is bulk density of pore fluid (kg/m^3), φ is friction angle between solid grains (°).

In this study, *Fr* values were set to vary between 2.47 to 5.01, which is within the range of values obtained for natural channelized debris flow events (0.45~7.56) (cf. McArdell et al., 2007; Hübl et al., 2009; Kwan et al., 2015; Zhou et al., 2019a). It is acknowledged that the subcritical Froude condition (*Fr*<1) was not achieved due to inherent limitation of small-scale experiments which only allow limited initial volumes and shallow flow depths (Choi et al., 2015). A compilation of dimensionless numbers obtained for the cases in this study, natural debris-flow events (Iverson, 1997a; Iverson and Vallance, 2001), large-scale (Iverson, 1997a), and other small-scale flume experiments (Iverson and Vallance, 2001; Haas et al., 2015; Zhou et al., 2019b) is provided in Table 2.

2.2 *Experimental setup*

The experimental tests in this study were conducted using a new instrumented model flume. Figure 2 (a) shows a photograph of rectangular model flume, which consists of a storage tank, a rectangular channel with two different inclinations, and a recycling pool. Figures 2 (b) and 2(c) show the side view and plan view of the model flume, respectively, with an overall length of 10.2m, a base width of 0.3m, and a depth of 0.8m. The storage tank is 1.0m long, with a maximum capacity of 0.17m^3 when inclined at 25°.

In order to replicate real debris flows, a flume with two different inclinations – a steep upper channel and a less inclined lower channel – is used (Zhou et al., 2019a). The upper 3.2m of the channel is regarded as the acceleration transportation zone which is inclined at 15° or 25° (θ_1). The lower 6.0m of the channel is regarded as the deceleration deposition zone which is fixed at 5° (θ_2). The channel bed is made of steel plate which is roughened by gluing a layer of fine debris to its surface. Transparent sidewalls were made out of 3.0m long Perspex, which enabled us to observe the interaction process between the debris flows and model dams.

350mm tall modelled slit dams (or check dam) were installed perpendicular to the channel bed, 1.65m downstream of the junction between the upper and lower channel (Figs. 2b and 2c). The location of the model dams was determined as the downstream position in which targeted flow *Fr* between 2.5 to 5.0 can be achieved across different flow conditions. The main body of slit dam is usually comprised of a number of equally

192 spaced rigid posts (Chanson, 2004; Marchelli et al., 2019; Zhou et al., 2020). In this
193 study, the simplified model slit dams are comprised of one complete post which ranges
194 from 60mm to 114mm wide and two others which are half as wide positioned at the
195 sides (Fig. 2d). The corresponding slit size of the simplified model slit dams range from
196 36mm to 90mm and are varied by changing the thickness of the posts.

197 **2.3** ***Instrumentation and measurement***

198 A measurement module was embedded in the centerline of the flume bed 1.0m
199 downstream of the intersection between the upper and lower channel (Figs. 2b and 2c).
200 The surface of the measurement module was flush with the flume bed surface. The
201 measurement module is comprised of a load cell (named as "LC", LH-SZ-02 range
202 from 0 to 50N, with accuracy of 0.1%), and a rapid response differential pore-fluid-
203 pressure transducer (named as "PPT", OMEGA-PX409-001G5V, range from 0 to 1PSI,
204 with accuracy of 0.08%) for measuring total basal normal stress (σ) and basal pore-
205 fluid pressure (u_w) at the base simultaneously which enables the characterization of
206 flow conditions during debris-flow motion. As to the measurement module
207 configuration, a circular plate with a diameter of 160mm is rigidly affixed to the load
208 cell and is free to deflect in the normal direction. The pore-fluid-pressure transducer is
209 connected through a port to another rigid steel plate adjacent to the load cell circular
210 plate (see, Fig. 2e; cf. Iverson, 1997a; Major and Iverson, 1999; Iverson et al., 2010).
211 The port was filled with the same fluid material used in the experiment and covered
212 with a 50-mesh screen to provide rapid and direct hydraulic connection to the pore fluid

213 at the base of the debris flow (cf. Iverson and LaHusen, 1989; Major and Iverson, 1999).

214 An ultrasonic distance sensor (named as “UDS”, Banner-U-GAGE T30U Series,
215 range from 0 to 1m, response time in 48ms) with a resolution of 0.1mm suspended over
216 the measurement module in the model flume precisely measures the temporal variations
217 of the depth of the moving debris flow (Iverson, 1997a; Major and Iverson, 1999). Five
218 impact force sensors (see Fig. 2d, named as “FS1” to “FS5”. LH-Y127B, range 0~200N,
219 with accuracy of 0.15%) with diameter of 28mm were embedded along the height of
220 the model dams. Their locations on the dam are shown in Fig2c. The surface of impact
221 force sensors was flush with the model dam surface. As the most drastic changes of
222 impact pressure occurs during the debris flow frontal impact at the dam base, the bottom
223 of the dam is intensively instrumented. Sensor signals mentioned above were logged
224 by computers at rates of 500 Hz.

225 In addition, the interaction process between the debris flows and dams was filmed
226 using a high-speed camera (Photron FASTCAM Mini UX50) with a resolution of
227 1280×1024 pixels sampled at a frequency of 250 frames per second (fps). Illumination
228 was provided by two 1000W light-emitting diodes (LED). Reference lines, with
229 intervals of 0.01 m, were drawn at the side-base of the channel to approximately
230 estimate the frontal velocity of the flow.

231 **2.4** ***Materials, program, and testing procedures***

232 In this study, the prototype debris flows are simplified as ideal two-phase flows of
233 non-uniform granular materials and a viscous pore fluid. Figure 3 shows the materials

234 used in the tests. The non-uniform cobblestones are used to model the granular material
235 of debris flows. Glass beads with diameters of 0.4~0.6mm were used to model the fine
236 debris. The viscous liquid adopted in this study was a mixture of glycerol and water.
237 Glycerol was used for its transparence, high solubility, and viscosity. The density of the
238 viscous fluid was about 1200 kg/m³ and its viscosity was 0.05 Pa·s measured using a
239 Physica MCR301 torque rheometer. The grain-size distribution of the solid materials
240 used for the tests is shown in Fig. 4. The maximum diameter (D_{max}) of the granular
241 material is 20 mm and the median size (d_{50}) is 3.7 mm. The bulk density of solid
242 material was measured as 2747 kg/m³ . The interface friction angle between the granular
243 materials and the channel-bed was measured as 33.5° obtained through tilting tests
244 (Savage and Hutter, 1989).

245 Slit size (b) and solid fraction (C_s) were varied to discern their influence on the
246 impact load on the model dams. Five relative slit sizes (b/D_{max}) were studied: 0 (*i.e.*,
247 check dam), 1.8, 2.3, 3.6, and 4.5. Solid fractions of 0.4 and 0.6, which correspond to
248 bulk densities of 1819 kg/m³ and 2128 kg/m³, respectively, were adopted since C_s
249 values of natural debris flows typically range from 0.4 to 0.8 (Iverson, 1997a; Iverson
250 and George, 2014; Song et al., 2017). Details of twenty-four tests are summarized in
251 Table 3. Prior to conducting impact tests, a series of reference tests without the dams
252 were first carried out. The reference tests have IDs marked with “R”, the tests using
253 check dams (b/D_{max}=0) are marked with “C”, and the tests with slit dams marked with
254 “S”, respectively.

In the reference tests, the dimensionless group was calibrated based on the measured velocities and flow depths at the location where the dam would be later installed. The impact tests with dam were then carried out. After the flume model preparation, 0.05m³ granular-fluid mixtures were poured into the storage tank. The channel bed was wetted by the same fluid used in tests to model wet ground. To prevent consolidation of the experimental materials prepared in the storage tank, a hand-held electric mixer continuously stirred until the tank gate was pulled-up vertically as rapid as possible. The data logger and high-speed camera are triggered when the tank gate is released. The granular-fluid mixtures rapidly elongate and thin out as they move downslope along the channel.

2.5 *Data processing*

Previous studies have revealed that the impact pressure of debris flows is a superposition of the hydraulic impact pressure (caused by slurry and fine debris) and boulder impact pressure (Mizuyama, 1979; Miyoshi, 1990; Hu et al., 2011, Cui et al., 2015; Yan et al., 2020). The large boulder impulse load easily results in the local damage of countermeasure structures. However, the whole overturning and slipping of structures are usually caused by the continuous hydraulic impact pressure. In this study, the long-term smooth component of the impact pressure is studied, which is regarded as continuous hydraulic impact pressure. The original signal includes noise resulting from the measuring system, external disturbances and sensor vibration due to impact. The noise and the signals caused by dispersed particles can be filtered using the moving

276 average method (10 points were adopted) after filtering out the more extreme impact
277 signals. (cf. Hu et al., 2011; Kaitna et al., 2016). Figure 5 shows the original and filtered
278 impact pressures recorded by the impact force sensor "FS1" in the tests S15-0.4-4.5 and
279 S25-0.6-4.5.

280 3. Experimental results of impact tests

281 3.1 *Properties of incoming flows*

282 Measurements of relevant flow properties such as the flow depth (h), total basal
283 normal stress (σ), and basal pore-fluid pressure (u_w) of the incoming flow, obtained
284 simultaneously 0.65 meters upstream of the model dams are shown in Fig. 6. To
285 facilitate comparison, the initial time of the data logger is readjusted to 1.0s before the
286 flow front arrives at the sensor plate. A tapered debris flow front approaches the dam
287 location at which the maximum flow height is measured. Total basal normal stress
288 varies proportionately with flow depth. On the other hand, the increase of the basal
289 pore-fluid pressure lagged indistinctively behind the abrupt changes of total basal
290 normal stress.

291 The ratio between the basal pore-fluid pressure and the total basal normal stress
292 (u_w/σ) is illustrated in Fig. 6(d). Modelled debris flows with C_s=0.4 have u_w/σ values
293 which are even slightly larger than 1. It means that flows with low solid fractions are
294 completely liquefied. Flows with C_s=0.6 on the other hand have u_w/σ values which are
295 either less than or approximately equal to 1, implying that although the flow is liquefied
296 to some extent, particle contact interactions in transport mechanisms are stronger than

297 that in flows with C_s=0.4. The degree of liquefaction can be compared between the
298 modelled debris flows by the value of u_w/σ. Note that the basal pore-fluid pressure
299 slightly exceed threshold sufficient to liquefy the debris during movement, which may
300 be caused by minor drift of either the load cell or pore water pressure sensor calibration.
301 These results are similar to the ones obtained by Iverson (1997a; 1997b), Major and
302 Iverson (1999). More details about the properties of the incoming flows are summarized
303 in Table 3.

304 **3.2** ***Observed impact kinematics***

305 In this section, the impact process of debris flows against slit dams is examined. It
306 was found from the high-speed images that the impact characteristics for a single b/D_{max}
307 ratio are generally identical regardless of the flume angle of inclination. Thus, the
308 impact characteristics of debris flows on slit dams with different b/D_{max} (*i.e.*,
309 b/D_{max}=1.8 and =4.5) for C_s=0.4 and C_s=0.6, respectively at a constant flume inclination
310 of 15° are shown in Figs 7 and 8.

311 Figures 7(a) and 7(b) show modelled debris flows S15-0.4-1.8 and S15-0.4-4.5
312 approach the slit dams with frontal velocities of about 2.0m/s (Fig. $7a_1$ and b_1). During
313 the impact process, thin run-up layers develop along the front surface of the slit dams
314 and the weak dead zone forms (Figs. $7a_2$ and b_2). A visible jet flow forms as the
315 granular-fluid mixture tries to pass through the slit dam with narrow relative slit size
316 (b/D_{max}=1.8) (Figs. $7a_2$-a_4) . Wide slit dams (b/D_{max}=4.5) on the other hand, allow most
317 of the granular-fluid mixture to pass through with minimal jet flow during run-up (Figs.

318 7b_2-b_4). These distinct impact characteristics persist even at maximum flow depth (Fig.
319 7a_4 and Fig. 7b_4). At the end of the run-up process, the granular-fluid mixtures detained
320 by the narrow slit dam are slowly discharged (Fig. 7a_5) whereas, at this stage, a steady
321 flow height is already achieved at the front and backside of the dam as the large slit size
322 barely retains the incoming flow (Fig. 7b_5). The debris flows eventually stop at
323 t=8.612s (Fig. 7a_6) and t=7.512s (Fig. 7b_6) for the narrow and widely spaced slit dams
324 respectively.

325 Flows with higher solid fractions impact the dams at lower flow velocities of about
326 1.4m/s (Figs. 8a_1 and 8b_1) which result to lower flow kinetic energies and less
327 pronounced run-up heights (Figs. 8a_2-a_4 and 8b_2-b_4). Weak dead zone can be observed
328 in the test S15-0.6-1.8, while almost no dead zone can be found in the test S15-0.6-4.5.
329 Large fractions of the mixtures are retained behind the dams since a higher solid
330 fraction means more particles are available to create heaps and clusters which
331 effectively block the dam opening (Figs. 8a_5 and 8b_5). As more energy is dissipated due
332 to particle contact, the debris flows eventually stop at shorter times at t=5.532s (Fig.
333 8a_6) and t=4.472s (Fig. 8b_6). More details about impact characteristics between debris
334 flows and slit dams can be found in the paper reported by Zhou et al. (2019a).

335 **3.3** ***Evolution of impact pressure***

336 The pressure distribution along the dam height is essential to obtain the total
337 impact load against the mitigation structure. The evolution of impact pressures
338 measured at five different points along the height (labelled FS1 to FS5) of tests C15-

339 0.4-0 (check dam) and S15-0.4-4.5 are shown in Figs. 9 (a) and 9(b). The initial time
340 of the FS1 is readjusted to t=0.25s before the flow front impacting the dams.

341 For check dams (Fig. 9a) maximum pressures are measured at the bottom sensor
342 (FS1) characterized by a sharp impulse (0.308s following the initial impact) which then
343 rapidly decreases prior to settling at a constant value. The maximum impact pressure
344 measured by the second sensor FS2 is slightly lower and later in time than that detected
345 by FS1. The pressure behind the maximum value is even larger than that detected by
346 FS1 over a certain period of time. The top sensors (FS3~FS5), due to the low flow
347 height, only measure the run-up impact pressures. It should be noted that a second,
348 lower magnitude, pressure spike can be observed near the end of the signals measured
349 by all sensors. As observed in high-speed images, this is caused by the trailing waves
350 which arrive at the dam near the end of run-up process.

351 In slit dams, the largest impact pressures are also measured at the bottom force
352 sensor FS1 wherein the maximum value is recorded 0.256s after the initial impact.
353 However, there is an obvious discrepancy between the pressures measured by FS1 from
354 those recorded by sensors FS2~FS5. This reflects the weak run-up as most of mixtures
355 simply pass through the wider slit size. It should also be noted that although the impact
356 profile is comparable in magnitude to that of the check dam, it is not as sharp and is
357 instead distributed over a longer span of time. The second peak pressure recorded in
358 check dams is also not observed in widely spaced slit dams as trailing waves can easily
359 exit through the slits.

To further highlight the influence of the slit size (b) on the impact pressure distribution along the dams, the impact pressures detected by the force sensors FS1 and FS2 for mixtures with low solid fraction C_s=0.4 flowing at θ_1=15° are shown in Figs. 9 (c) and 9(d) respectively. The shaded triangles represent the impact pressure impulse, which is defined as the impact pressure integrated over the impact time (Peregrine, 2003; Lobovský et al., 2014; Song et al., 2017), *i.e.*, time from initial impact up to the point when it settles to a constant value. To facilitate comparison, the impact pressure time histories recorded by FS1 are redistributed by resetting their initial times. Based on the size of the triangles, impact pressure impulse increases with slit size and is lowest in check dams. In addition, the difference between the rise time and decay time for the triangle also increases varying the b/D_{max}. However, in the range of $b/D_{max} \geq 3.6$, the values of impact pressure impulse are almost equal.

Contrary to the results in Fig. 9(c), the corresponding impact pressures measured by FS2 generally decreases with b/D_{max} (Fig. 9d). Except that the pressure in the test S15-0.4-1.8 is lower than that in the test S15-0.4-2.3, which is caused by the lower incoming flow velocity in the test S15-0.4-1.8. This once gain reflects the decrease of run-up as larger slit size allows for larger fractions of the mixture to exit freely. The influence of slit size on the impact pressure will be discussed in the following section.

4. Influence of slit size and solid fraction on impact load

Proper estimation of the potential impact loads exerted on slit dam and adopting reasonable slit size are key procedures to guarantee safe and effective operation for slit

dams. Although lots of studies about the estimation impact loads of debris flow have been reported, less attention has been paid to the slit size effect on the values of impact loads exerted by debris flow. To facilitate comparison, the check dam can be also classified as slit dam with b/D_{max}=0. In this section, the influence of slit size characterized by b/D_{max} on the maximum frontal impact pressure and the total impact force is investigated. In addition, the effect of debris flow solid fraction is studied.

4.1 *Frontal impact pressure*

In the current design practices, it is conventionally considered as the most critical impact scenario for debris-flow mitigation structures when the peak impact pressure (P_{peak}) occurs. The studies (Song et al., 2017) and the aforementioned results have shown that the peak impact pressure is always detected by the sensor at the base of the dams during the frontal impact. Thus, the peak frontal impact pressure recorded by FS1 is adopted to back-calculate the empirical dynamic pressure coefficient value for each test. To facilitate comparison, the empirical dynamic pressure coefficient deduced by the peak frontal pressure is denoted as α_1, *i.e.*, $\alpha_1=P_{peak}/\rho v^2$. The relationship of the α_1 with the relative slit size (b/D_{max}) is plotted in Fig. 10(a). The error bars are adopted to account for the uncertainty caused by the measured flow velocity. Three reference lines with different lengths (*i.e.*, 10cm, 20cm, and 30cm) are used to estimate the flow velocities. The α_1 value is deduced based on the average velocity measured in the experiments, and the its minimum and maximum values are represented by the upper error line and lower error line, respectively in Fig. 10(a).

Theoretically, normalized maximum frontal pressures should be unity for flowing

403 sediments without a static component acting on the dam. However, Fig. 10(a) shows
404 that all α_1 values are less than unity. This is because the flow momentum upon impact
405 is transferred vertically along the surface of the dams due to the predominantly run-up
406 mechanism, rather than as concentrated loading impact the base of dams (Song et al.,
407 2017). Besides, the particles rearrangement (contraction) at the dispersed flow front
408 may also lead to smaller α_1 values than unity. Fig.10(a) illustrates that α_1 is weakly
409 dependent on the relative slit size (b/D_{max}) for all tests. Specifically, the deviation range
410 of the α_1 values relative to the average value is about 7% ~ 8% in group of tests 15-0.4,
411 9% ~ 13% in group of tests 25-0.4, 13% ~ 16% in group of tests 15-0.6, and 15% ~ 17%
412 in group of tests 25-0.6. Consequently, it can be regarded that α_1 deduced from the peak
413 frontal impact pressure is almost unaffected by the slit size of debris-flow mitigation
414 dams, but is rather determined by the momentum of approaching debris flows.

415 **4.2** ***Total impact load exerted on slit dam***

416 In the hydro-dynamic approach, the frontal impact is usually considered as the
417 most critical situation for engineering design, due to the peak impact pressure occurs
418 during the frontal impact. However, Song et al. (2017) has demonstrated that regardless
419 of the variation of the flow solid fraction, the frontal impact of a run-up mechanism
420 only contributes less than 25% of the total impact force impulse. Besides, Cui et al.,
421 (2015) also pointed out that the impact pressure would be underestimated if only the
422 frontal impact is considered. In other words, the frontal impact is not critical for
423 engineering design when considering debris flow run-up. In fact, the peak impact force

(F_{peak}) exerted on the retention structures is a key parameter when investigating debris-barrier interaction. In this study, the total impact force exerted on the dams with unit width can be obtained through integration of the impact pressure distribution along the dam height.

As to the impact when the peak impact force (F_{peak}) occurs as the most critical scenario for mitigation structure design, the F_{peak} exerted on the dams with unit width is adopted to back-calculate the empirical dynamic pressure coefficient. It is normalized by the product of ρv^2 and flow depth. Thus, the empirical dynamic pressure coefficient deduced by the F_{peak} can be expressed as $\alpha_2=F_{peak}/\rho v^2 h$, in which the pressure coefficient includes both dynamic and static load during the impact process. The variation of α_2 with relative slit size b/D_{max} is shown in Fig.10(b). Likewise, the error bars of the α_2 value relative to the average values are shown. It can be seen that the α_2 values are obviously larger than the α_1 values, since it incorporates the static component contributed by weight of the retained debris flow materials. More importantly, compared with the α_1 values in Fig.10(a), the α_2 values show obvious variation with b/D_{max}.

Specifically, when $b/D_{max} \leq 1.8$, the slit size makes little influence on the α_2 value. The result indicates that slit dams with $b/D_{max} \leq 1.8$ behave like a check dam ($b/D_{max}=0$), in terms of its ability to retain debris flows (*i.e.*, flows cannot freely pass through narrow slits). Increasing b/D_{max} from 1.8 to 3.6, it can be observed that the α_2 value decreases almost linearly with the b/D_{max}. The α_2 value is reduced by 23% for the tests with $C_s=0.4$,

445 while 30%~40% for the tests with C_s=0.6. However, as b/D_{max} is further increased, *i.e.*,
446 lager than 3.6, the α_2 value remains unchanged. This implies that for the considered
447 range of b/D_{max}, the b/D_{max}=3.6 can be regarded as a critical value for design of slit
448 dams. In other words, dams with b/D_{max}>3.6 offer practically negligible resistance to
449 incoming flow and will allow most of the material to pass through. Thus, little static
450 component contributed by weight of the retained debris flow materials exerts on slit
451 dams. To sum up, the slit size of debris-flow mitigation dams should be considered
452 when estimating the impact load of debris flow.

453 **4.3** ***Influence of the incoming-flow properties on impact load***

454 Previous works have illustrated that the impact load exerted on countermeasure
455 structures can be influenced by the incoming-flow properties (Proske et al., 2011; Song
456 et al., 2017), such as the flow velocity and the solid fraction, etc. In this study, the
457 properties of the incoming flow are controlled by the solid fraction and the flume
458 inclination (θ_1). The Froude number (*Fr*) is adopted to characterize the flow property,
459 which eliminate the discrepancy of flow properties caused by solo factor of flow solid
460 fraction or flume inclination. The relationship between the deduced empirical dynamic
461 pressure coefficient (α_1) and the *Fr* is plotted in Fig. 11 (a). It is also compared with the
462 previous experimental or field monitoring results obtained by the flow front impacting
463 a slit structure or a rigid post. (Zhang and Yuan 1985; Hübl and Holzinger 2003; Proske
464 et al. 2011; Cui et al. 2015). It can be found the trend of the α_1 value decreasing with
465 the *Fr* in inverse proportional function way. It decreases rapidly when the *Fr* is in the

range of 0 to 2, while it is less dependency of the α_1 when the *Fr* increases above 2. The α_1 value obtained in this study is also in accordance with this tendency regardless of the flow solid fraction or the flume inclination. It can be further seen from the inset in Fig. 11 (a) that lager flume inclination leads to lager *Fr*, thus a little bit smaller α_1 value obtained for the tests with the same solid fraction.

The Fig. 10 (a) also shown that the α_1 values are larger for the tests with smaller solid fraction (C_s=0.4) when the flume inclination and relative slit size are same. The results indicate that the dynamic component contributed by inertia dominates for the tests with C_s=0.4 during the impact process, while the static component contributed by gravity dominates for the tests with C_s=0.6 (cf. Song et al., 2017). It can be further corroborated by the values of Savage number (N_{Sav}) shown in Fig. 11(b). The lager N_{Sav} value for the tests with C_s=0.4, which means the flow with more momentum and the larger inertial stress from grain collision during the impact process than that in the tests with C_s=0.6 which with lager stress from solids contact friction.

4.4 *Effect of slit size on the variation of flow regimes during the debris-flow impact*

Debris flows, prior to impact model dams, are usually characterized according to their velocities, flow depths, basal pore-fluid pressures, etc. The change of these flow parameters following the mixtures' impact on retaining structure are difficult to obtain in detail due to the dispersion of the flow front. In this study, the flow depth, basal pore-fluid pressure, and total basal normal stress of the flow body at 0.65 meters upstream the dam location were measured using the sensor plate during whole impact process.

Those parameters of flow body following the flow front can be adopted to indirectly interpret the impact behaviors. As stated in section 3.1, although the basal pore-fluid pressure slightly exceeds the threshold sufficient to fully liquefy the flow, the value of u_w/σ can still be used to compare the relative mobility of debris flows.

As illustrated in Fig. 12, the time history of the u_w/σ in the series of tests 15-0.4 and 15-0.6 are plotted. The initial time is readjusted to 1.0s before the flow front arrives at the sensor plate. For the reference test R15-0.4-nd and S15-0.4-4.5, the flow bodies are almost fully liquefied during the whole flow process. While, as the b/D_{max} decreases from 3.6 to 0, the duration of liquefied condition of the flow body is decreased. The similar tendency is also shown in the series of tests 15-0.6. The results imply that when the $b/D_{max} \leq 3.6$, the slit dam promotes the consolidation of the granular mixtures of the flow front. Then, it promotes the deposition of solid particles propagating from the flow front to the rest of the body. The solid particles of the body reach static conditions quicker with decreasing b/D_{max}. As the granular mixtures consolidate, the flow mobility also attenuates as the total basal normal stress increases. The experimental results further corroborate that $b/D_{max}=3.6$ is a critical value for the slit dam to effectively mitigate debris-flow hazards.

5. Impact pressure distribution models on countermeasure structures

Apart from the magnitude of impact pressure, the impact pressure distribution on the mitigation structures is also a key aspect to estimate the total impact load by integration of pressures along the dam height, and its evolution varying time can also

508 contribute to insight on the debris flow impact. In this study, the characteristics of
509 measured pressure distributions against on the model dams will be first discussed, and
510 its corresponding simplified pressure distribution models will also be proposed. Then,
511 the proposed pressure distribution models in this study will be compared with those
512 from the existing guidelines and literatures.

513 **5.1** ***Distribution of impact pressure on slit dams***

514 To obtain a clearer picture of how pressures are distributed within the dam, the
515 pressure distribution of tests with C_s=0.4 and C_s=0.6, for different values of b/D_{max} are
516 plotted in Fig. 13. These distributions are obtained at the occurrence of the peak
517 pressure, peak force, and until static conditions within the span of the impact time. The
518 height (H) of the impact force sensors on the model dam are normalized by the flow
519 depth (h) and the corresponding pressure values detected are normalized by ρv^2.

520 The peak impact pressure in test C15-0.4-0 was detected at base of the check dam
521 by FS1, which occurred at t=0.308s during the frontal impact process (Fig. 13a). As
522 time progresses, the impact pressures shift upwards decreasing the pressures at the
523 bottom of the dam (Fig. 13a, t=0.400s). At the time when the peak force is measured
524 (t=0.478s), the impact pressure detected by FS2 is larger than that recorded by FS1. By
525 the end of impact process (t=1.19~1.9s) the impact pressure distribution along the dam
526 height is found to be triangular. The high-speed images during the impact process show
527 that a layer of run-up develops along the surface of the dam during which a fraction of
528 the solid particles deposit at the bottom of the dam to form a dead zone. As run-up
529 proceeds, the trajectory of incoming flow deflects upward along the surface of the

530 expanding dead zone (see Fig.7a). Thus, it can be inferred that the maximum impact
531 pressure shift upwards from FS1 to FS2 is caused by the formation and expansion of
532 the dead zone. During the run-up impact process, the main kinetic energy of debris flow
533 was converted into potential energy, and the flow direction is parallel to surface of the
534 dam, which leads to relatively small impact pressure exerted on the upper part of the
535 dam.

536 FS1 frontal impact pressure readings of slit dams with b/D_{max}=1.8 (Fig. 13b) are
537 almost identical to those in check dams. Similarly, at the time when the peak force is
538 recorded (t=0.648s), FS2 readings are greater than in FS1 but are both generally lower
539 in magnitude. This feature is no longer observable in b/D_{max}=3.6 (Fig. 13c) in which all
540 measured pressures at all times are significantly attenuated. Having FS1 readings which
541 are higher than FS2 at the peak-force time indicates that the dam base absorbs most of
542 the impact since no or weak basal structure (*i.e.*, dead zone) forms to attenuate the
543 impact force. These results further indicate that for larger slit size, more debris flow can
544 directly pass through the slit dam leading to lesser dead zone formation, attenuated run-
545 up process, and lower pressure readings on the upper part of structure.

546 Compared to the tests with C_s=0.4, the series of tests that debris flows with C_s=0.6
547 impacting on the check dam and slit dams take shorter time to reach static conditions
548 due to lower frontal velocity and stronger grain contact friction. Similarly, the
549 maximum impact pressures also occurred during the frontal impact in each test, and the
550 normalized maximum impact pressure almost equals for the tests of C15-0.6-0 and S15-

551 0.6-1.8, and lower for the test of S15-0.6-3.6. Likewise, the decreasing tendency also
552 occurs that impact pressure exerted on the upper of dams with increasing of the slit size.
553 In general, the frontal impact pressure in the tests with C_s=0.6 is less than that in the
554 tests with C_s=0.4. This is because the static load is dominant for the tests with C_s=0.6
555 during the impact process instead of the impact load (Song et al., 2017).

556 **5.2** ***Comparison of the impact pressure distribution models on countermeasure***
557 ***structures***

558 Studies have been shown that the pressure distribution pattern is also heavily
559 influenced by the structure type (Hübl et al., 2009; Proske et al., 2011; Song et al., 2017).
560 In this section, based on the measured pressure distributions in this study, the new
561 bilinear distribution models are proposed for both check dam and slit dam. The existing
562 impact pressure distribution from existing guidelines and literatures are also presented.
563 All the impact pressure distribution models discussed in this study are shown in Fig.
564 14.

565 As shown in Figs. 14a_1-a_3, the conventional pressure distribution models for
566 closed-type dam (e.g., check dam) include the triangle, trapezoid, and rectangle model
567 (WLV, 2006; Hübl et al., 2009; Suda et al., 2009 and 2010; Proske et al., 2011). The
568 triangular pressure distribution model is adopted when the hydrostatic approach is used
569 to estimate the impact load of debris flows, in which the pressure is caused by the
570 weight of the static component. For the hydro-dynamic approach, the trapezoidal model
571 with the bottom edge denoting peak impact pressure and top edge denoting 0.25 times
572 the peak pressure (Fig.14 a_2), or the rectangular model with uniform peak pressure from

573 the bottom to the top (Fig.14 a_3) is adopted to estimate the impact load. In the
574 conventional pressure distribution models, the height of the dam (H_{max}) is treated as the
575 flow depth (h) and the peak impact pressure is regarded as the maximum design value.
576 In current practice, the pressure distribution models are on the conservative side for the
577 design of closed-type dams without consideration of load attenuation from the debris-
578 structure interaction (Koo et al., 2017). Based on the physical test results and the energy
579 dissipation which results from the run-up impact process, Song et al. (2017) proposed
580 a revised triangular pressure distribution model for rigid barriers at the point when the
581 peak force and maximum bending moment are measured (Fig. 14b). In this model, the
582 maximum pressure of the triangular distribution is about 0.7 times the measured peak
583 impact pressure which is measured during frontal impact. In addition, the run-up height
584 is also considered in this model.

585 For open-type dams (e.g., slit dam), Suda et al. (2009, 2010) analyzed the
586 experimental results from the miniaturized tests conducted by Hübl and Holzinger
587 (2003), and proposed a double rectangular pressure distribution model (Fig. 14c_1) for
588 the granular debris flow and a bilinear trapezoidal distribution model (Fig. 14c_2) for
589 muddy debris flows. As shown in Fig. 14c_1, the uniform peak pressure is distributed
590 from the bottom to 0.4 of the dam height, and 0.5 times peak pressure is evenly
591 distributed on the upper part of dam. As illustrated in Fig. 14c_2, the peak impact
592 pressure occurs at the bottom edge of the bilinear trapezoid. At the 0.7 of the dam height,
593 the pressure value is reduced to 0.15 times the peak impact pressure, and 0.05 times the

peak impact pressure for the top edge. Test results show that the deposition height reaches the top of the dam in the test with granular debris flow. Thus, the pressure on the upper of dam is relatively larger compared to that in the test with muddy debris flows impact. Moreover, based on experimental results and considering the impact process, Cui et al. (2015) also reported pressure distributions of debris flows impacting a rigid post. As shown in Fig.14d, an inverse trapezoid pressure distribution is represented at the most critical impact scenario.

In this study, debris flows impacting on check dam and slit dams are investigated, in which new bilinear distribution models are proposed (Figs. 14e$_1$ and 14e$_2$). In the tests, the maximum normalized pressure is about $0.8\rho v^2$ at the base of the dam. Considering the energy dissipation caused by the formation of dead zones and the contact friction between the solid particles, the $0.7\rho v^2$ is adopted at the most critical impact scenario for the check dam and slit dam with $b/D_{max}\leq 1.8$ and $0.6\rho v^2$ is adopted for the slit dam with $b/D_{max}>1.8$. Hence, for simplicity, $0.85P_{peak}$ ($\approx 0.7/0.8$) and $0.75P_{peak}$ ($=0.6/0.8$) are adopted to characterize the bottom edge of the simplified pressure distribution model. For the test with check dam and slit dam with $b/D_{max}\leq 1.8$, the turning point of pressure is $0.25P_{peak}$ at the height of $3.5h$ (Fig. 14e$_1$). However, when the debris flow interacts with the slit dams with $b/D_{max}>1.8$, the run-up process becomes weaker because of the slit size allowing parts of flow materials passing through the slit dams. Hence, the turning point of pressure reduces to $0.2P_{peak}$ and its location also drops down to the $2.5h$ (Fig. 14e$_2$).

615 The configuration of the model dam in this study is almost vertical from the base
616 of the flume. As the modelled debris flows are thin and fast, and the dams are relatively
617 higher, the debris flows show a distinct run-up mechanism during the impact process,
618 which leads to the trajectory of incoming flow be deflected and parallel to the surface
619 of the dams. Thus, the measured pressure on the upper portion of the dam is obviously
620 smaller than that on the base. Similar results were also demonstrated by Armanini et al
621 (2019). To some extent, the proposed simplified pressure distribution models are
622 conventional based on the measured impact pressure in this study. Nevertheless, the
623 new models will lead to significant reduction of construction cost compared with the
624 traditional pressure distribution models. It is acknowledged that the proposed models
625 in this study can only be used for empty dams in which case the run-up mechanism
626 dominates as the debris flow impacts the dams. The bilinear pressure distribution
627 models need to be further studied in other situations.

628 ## 6. *Conclusions*

629 A series of physical modeling tests of debris flow impacting on check dams and
630 slit dams were carried out to study the influence of slit size on the impact loads. The
631 following conclusions can be drawn based on this experimental study:

632 (1) The peak impact pressure of debris flow usually occurs during the frontal impact.
633 The relative slit size (b/D_{max}) makes negligible difference on the peak frontal
634 pressure values. It indicates that the peak frontal pressure is largely unaffected by
635 the slit size of countermeasure structures instead of by the incoming flow properties.

(2) Considering the contribution of the static component caused by the gravity to the impact load, the slit sizes of the countermeasure structures make significant influence on the peak impact force exerted on the structures, which is regarded as the most critical design scenario. More specifically, as the b/D_{max} is increased from 1.8 to 3.6, the normalized total impact force unit width (α_2) is reduced by 23% for the tests with C_s=0.4, while 30%~40 for the tests with C_s=0.6. However, when the slit size becomes b/D_{max}>3.6, the α_2 value no longer changes.

(3) In addition, the experimental results imply that when the $b/D_{max}\leq$3.6, the slit dam promotes the consolidation of the granular mixtures propagating from the flow front to the rest of the body. It further corroborates that b/D_{max}=3.6 is a critical value for the slit dam to effectively mitigate debris-flow hazards.

(4) Based on the measured impact pressures distributed on the modelled check dam and slit dam, new bilinear distribution models are proposed. Those models are suitable for the debris flow impacts empty dams in which case the run-up mechanism dominates. The new models may lead to significant reduction of construction cost compared with the traditional pressure distribution models.

Acknowledgments

The authors acknowledge the financial supports from the CAS "Light of West China" Program, the National Natural Science Foundation of China (grant No. 51809261), and the International Science & Technology Cooperation Program of China (No. 2018YFE0100100). The financial support from research grant T22-603/15-N

657 provided by the Research Grants Council of the Government of Hong Kong SAR,
658 China is also greatly appreciated.

659 ***References***

660 Armanini, A., Larcher, M., Odorizzi, M., 2011. Dynamic impact of a debris flow front
661 against a vertical wall. In Proceedings of the 5th International Conference on Debris-
662 Flow Hazards Mitigation: Mechanics, Prediction and Assessment, pp.1041-1049
663 Padua, Italy.
664 Armanini, A., Rossi, G., Larcher, M., 2019. Dynamic impact of a water and sediments
665 surge against a rigid wall. J. Hydraul. Res. 1-12.
666 Baldwin, J.E., Donley, H.F., Howard, T.R., 1987. On debris flow/avalanche mitigation
667 and control, San Francisco Bay area, California. Debris Flows/Avalanches: Process,
668 Recognition, and Mitigation. Geological Society of America Reviews in Engineering
669 Geology 7, 223-236.
670 Bugnion, L., McArdell, B.W., Bartelt, P., Wendeler, C., 2012. Measurements of
671 hillslope debris flow impact pressure on obstacles. Landslides 9 (2), 179-187.
672 Canelli, L., Ferrero, A.M., Migliazza, M., Segalini, A., 2012. Debris flow risk
673 mitigation by the means of rigid and flexible barriers-experimental tests and impact
674 analysis, Nat. Hazards Earth Syst. Sci. 12, 1693-1699.
675 Chanson, H., 2004. Sabo check dams-mountain protection systems in Japan. Int. J. Riv.
676 Bas. Man. 2 (4), 301-307.
677 Chen, H.X., Li, J., Feng, S.J., Gao, H.Y., Zhang, D.M., 2019. Simulation of interactions
678 between debris flow and check dams on three-dimensional terrain. Eng. Geol. 251,
679 48-62.
680 Chen, X.Q., Cui, P., You, Y., Chen, J.G., Li, D.J., 2015. Engineering measures for
681 debris
682 flow hazard mitigation in the Wenchuan earthquake area. Eng. Geol. 194, 73-85.
683 Choi, C.E., Ng, C.W.W., Song, D., Kwan, J.H.S., Shiu, H.Y.K., Ho, K.K.S., Koo,
684 R.C.H., 2014. Flume investigation of landslide debris-resisting baffles. Can. Geotech.
685 J. 51 (5), 540-553.
686 Choi, C.E., Ng, C.W.W., Au-Yeung, S.C.H., Goodwin, G., 2015. Froude scaling of
687 landslide debris in flume modelling. Landslides 12 (6), 1197-1206.
688 Choi, S.K., Lee, J.M., Kwon, T.H., 2018. Effect of slit-type barrier on characteristics
689 of water-dominant debris flows: small-scale physical modeling. Landslides 15 (1),
690 111-122.
691 Cui, P., Zeng, C., Lei, Y., 2015. Experimental analysis on the impact force of viscous

692 debris flow. Int. J. Sediment Res. 40 (12), 1644-1655.
693 Cui, Y., Choi, C.E., Liu, H., Ng, C.W.W., 2018. Effects of Particle Size of
694 monodispersed granular flows impacting a rigid barrier. Nat. Hazards 91 (3), 1179-
695 1201.
696 Ferrero, A.M., Segalini, A., Umili, G., 2015. Experimental tests for the application of
697 an analytical model for flexible debris flow barrier design. Eng. Geol. 185, 33-42.
698 Gao, L., Zhang, L.M., Chen, H.X., 2017. Two-dimensional simulation of debris flow
699 impact pressures on buildings. Eng. Geol. 226, 236-244.
700 Haas, T., Braat, L., Leuven, J.R., Lokhorst, I.R., Kleinhans, M.G., 2015. Effects of
701 debris flow composition on runout, depositional mechanisms, and deposit
702 morphology in laboratory experiments. J. Geophys. Res.-Earth Surf. 120, 1949-1972.
703 Holsapple, K.A., 1993. The scaling of impact processes in planetary sciences. Annu.
704 Rev. Earth Planet. Sci. 21, 333-373.
705 Hong, Y., Wang, J.P., Li, D.Q., Cao, Z.J., Ng, C.W.W., Cui, P., 2015. Statistical and
706 probabilistic analyses of impact pressure and discharge of debris flow from 139
707 events during 1961 and 2000 at Jiangjia Ravine, China. Eng. Geol. 187, 122-134.
708 Hu, K., Wei, F., Li, Y., 2011. Real-time measurement and preliminary analysis of
709 debris-flow impact force at Jiangjia Ravine, China. Earth Surf. Process. Landf. 36
710 (9), 1268-1278.
711 Hübl, J., and Holzinger, G., 2003. Entwicklung von Grundlagen zur Dimensionierung
712 kronenoffener Bauwerke für die Geschiebebewirtschaftung in Wildbächen:
713 Klassifikation von Wildbachsperren, WLS Report 50. Im Auftrag des BMLFUWVC
714 7a (unveröffentlicht).
715 Hübl, J., Fiebiger, G., 2005. Debris-flow mitigation measures. In Debris-flow hazards
716 and related phenomena. Springer Berlin Heidelberg, pp: 445-487.
717 Hübl, J., Suda, J., Proske, D., 2009. Debris flow impact estimation. Proceedings of the
718 11th international symposium on water management and hydraulic engineering, pp.
719 1-4. Ohrid, Macedonia.
720 Hungr, O., Morgan, G.C., Kellerhals, R., 1984. Quantitative analysis of debris torrent
721 hazards for design of remedial measures. Can. Geotech. J. 21 (4), 663-677.
722 Huo, M., Zhou, J.W., Yang, X.G., & Zhou, H.W., 2017. Effects of a flexible net barrier
723 on the dynamic behaviors and interception of debris flows in mountainous areas. J.
724 Mt. Sci. 14 (10), 1903-1918.
725 Iverson, R.M., LaHusen, R.G., 1989. Dynamic pore-pressure fluctuations in rapidly
726 shearing granular materials: Science, v. 246, p. 796-799.
727 Iverson, R.M., 1997a. The physics of debris flows. Rev. Geophys. 34 (3), 244-296.

728 Iverson, R.M., 1997b. Hydraulic modeling of unsteady debris-flow surges with solid-
729 fluid interactions, in Chen, C. L., ed., Debris flow hazards mitigation: Mechanics,
730 prediction, and assessment: American Society of Civil Engineers, Proceedings of
731 First International Conference, August 7-9, San Francisco, p. 550-560.
732 Iverson, R.M., Vallance, J.W., 2001. New views of granular mass flows. Geology 29
733 (2):115-118.
734 Iverson, R.M., Denlinger, R.P., 2001. Flow of variably fluidized granular masses across
735 three dimensional terrain: 1. Coulomb mixture theory. J. Geophys. Res.-Solid Earth,
736 106 (B1), 537-552.
737 Iverson, R.M., Logan, M., Denlinger, R.P., 2004. Granular avalanches across irregular
738 three-dimensional terrain: 2. Experimental tests. J. Geophys. Res.-Solid Earth, 109
739 (F1).
740 Iverson, R.M., Logan, M., LaHusen, R.G., Berti, M., 2010. The perfect debris flow?
741 Aggregated results from 28 large-scale experiments. J. Geophys. Res.-Solid Earth,
742 115 (F3).
743 Iverson, R.M., George, D.L., 2014. A depth-averaged debris-flow model that includes
744 the effects of evolving dilatancy. I. Physical basis. Proc. R. Soc. London Ser. A-Math.
745 Phys. Eng. Sci. 470 (2170), 20130819.
746 Iverson, R.M., George, D.L., 2015. Modelling landslide liquefaction, mobility
747 bifurcation and the dynamics of the 2014 Oso disaster. Géotechnique 66 (3), 175-
748 187.
749 Jaeggi, M.N.R., Pellandini, S., 1997. Torrent check dams as a control measure for
750 debris flows. In Recent developments on debris flows. Springer, Berlin Heidelberg,
751 pp: 186-207.
752 Kaitna, R., Palucis, M.C., Yohannes, B., Hill, K. M., Dietrich, W. E., 2016. Effects of
753 coarse grain size distribution and fine particle content on pore fluid pressure and
754 shear behavior in experimental debris flows. J. Geophys. Res.-Earth Surf. 121 (2),
755 415-441.
756 Kattel, P., Kafle, J., Fischer, J. T., Mergili, M., Tuladhar, B. M., & Pudasaini, S. P.
757 (2018). Interaction of two-phase debris flow with obstacles. Eng. Geol. 242, 197-217.
758 Koo, R.C.H., Kwan, J.S.H., Ng, C.W.W., Lam, C., Choi, C.E., Song, D., Pun, W.K.,
759 2017. Velocity attenuation of debris flows and a new momentum-based load model
760 for rigid barriers. Landslides, 14 (2), 617-629.
761 Kwan, J.S.H., 2012. Supplementary technical guidance on design of rigid debris-
762 resisting barriers. GEO Report No. 270. Geotechnical Engineering Office, HKSAR
763 Government.
764 Kwan, J.S.H., Koo, R.C.H., Ng, C.W.W., 2015. Landslide mobility analysis for design

765 of multiple debris-resisting barriers. Can. Geotech. J. 1345-1359.
766 Leonardi, A., Calcagno, E., Pirulli, M., 2019a. Impact load estimation on retention
767 structures with the discrete element method. In Association of Environmental and
768 Engineering Geologists; Colorado School of Mines. Arthur Lakes Library, special
769 publication 28, 354-360.
770 Leonardi, A., Goodwin, G.R., Pirulli, M., 2019b. The force exerted by granular flows
771 on slit dams. Acta Geotech. 1-15.
772 Lin, X., Huo, M., Zhou, J.W., Cao, T., Yang, F.R., Zhou, H.W., 2017. An experimental
773 study on controlling post-earthquake debris flows using slit dams. Environ. Earth
774 Sci. 76 (22), 780.
775 Li, S., You, Y., Chen, X., Liu, J., Chen, J., 2019. Regulation effectiveness of a window-
776 check dam on debris flows. Eng. Geol. 253, 205-213.
777 Lo, D.O.K., 2000. Review of natural terrain landslide debris-resisting barrier design:
778 GEO report no. 104. Geotechnical Engineering Office, Civil Engineering
779 Department, The Government of Hong Kong Special Administrative Region.
780 Lobovský, L., Botia-Vera, E., Castellana, F., Mas-Soler, J., Souto-Iglesias, A., 2014.
781 Experimental investigation of dynamic pressure loads during dam break. J. Fluids
782 Struct. 48:407-434.
783 Major, J.J., 1997. Depositional processes in large-scale debris-flow experiments. J. of
784 Geol. 105(3), 345-366.
785 Major, J.J., Iverson, R.M., 1999. Debris-flow deposition: Effects of pore-fluid pressure
786 and friction concentrated at flow margins. Geol. Soc. Am. Bull. 111(10): 1424-1434.
787 Marchelli, M., Leonardi, A., Pirulli, M., Scavia, C., 2019. On the efficiency of slit-
788 check dams in retaining granular flows. Géotechnique, 1-12.
789 McArdell, B.W., Bartelt, P., Kowalski, J., 2007. Field observations of basal forces and
790 fluid pore pressure in a debris flow. Geophys. Res. Lett. 34 (7).
791 Miyoshi, L., 1990. Experimental study on impact load on a dam due to debris flow. The
792 XIX World Congress of the International Union of Forestry Research Organizations，
793 Montreal, Canada, August 5-11, 1990.
794 Mizuyama, T., 1979. Estimation of impact force on dam due to debris flow and its
795 problems. J. Jap. Society. Eros. Contr. Eng. 112, 40-43.
796 MLR (Ministry of Land and Resources), 2004. Design standards for debris flow hazard
797 mitigation measures (DZ/T0239-2004), Beijing, China: Chinese Geological Survey,
798 Ministry of Land and Resources (in Chinese).
799 Ng, C.W.W., Choi, C.E., Song, D., Kwan, J.H.S., Koo, R.C.H., Shiu, H.Y.K., Ho,
800 K.K.S., 2015. Physical modeling of baffles influence on landslide debris mobility.
801 Landslides 12 (1), 1-18.

802 Ng, C.W.W., Song, D., Choi, C.E., Liu, L.H.D., Kwan, J.S.H., Koo, R.C.H., Pun, W.K.,
803 2016. Impact mechanisms of granular and viscous flows on rigid and flexible barriers.
804 Can. Geotech. J. 54 (2), 188-206.
805 NILIM (National Institute for Land and Infrastructure Management), 2007. Manual of
806 technical standards for designing sabo facilities against debris flow and Driftwood,
807 Technical Note of NILIM No. 365. Tsukuba, Japan: Natural Institute for Land and
808 Infrastructure Management, Ministry of Land, Infrastructure and Transport (in
809 Japanese).
810 Parsons, A.J., Bracken, L., Poeppl, R.E., Wainwright, J., Keesstra, S.D., 2015.
811 Introduction to special issue on connectivity in water and sediment dynamics. Earth
812 Surf. Process. Landf. 40 (9), 1275-1277.
813 Peregrine, D.H., 2003. Water-wave impact on walls. Annu. Rev. Fluid Mech. 35 (1),
814 23-43.
815 Poudyal, S., Choi, C.E., Song, D., Zhou, G.G.D., Yune, C.Y., Cui, Y., Leonardi, A.,
816 Busslinger, M., Wendeler, C., Pition, G., Moase, E., Strouth, A., 2019. Review of
817 the mechanisms of debris-flow impact against barriers. In Association of
818 Environmental and Engineering Geologists; Colorado School of Mines. Arthur
819 Lakes Library. special publication 28, 1027-1304.
820 Proske, D., Suda, J., Hübl, J., 2011. Debris flow impact estimation for breakers. Georisk
821 5 (2), 143-155.
822 Savage, S.B., 1984. The mechanics of rapid granular flows. In Advances in applied
823 mechanics, Elsevier 24, 289-366.
824 Savage, S.B., Hutter, K., 1989. The motion of a finite mass of granular material down
825 a rough incline. J. Fluid Mech. 199, 177-215.
826 Shen, W., Zhao, T., Zhao, J., Dai, F., Zhou, G. G., 2018. Quantifying the impact of dry
827 debris flow against a rigid barrier by DEM analyses. Eng. Geol. 241, 86-96.
828 Song, D., Ng, C.W.W., Choi, C.E., Zhou, G.G.D. , Kwan, J.S.H., Koo, R.C.H., 2017.
829 Influence of debris flow solid fraction on rigid barrier impact. Can. Geotech. J. 54
830 (10), 1421-1434.
831 Song, D., Zhou, G.G.D., Xu, M., Choi, C.E., Li, S., Zheng, Y., 2019. Quantitative
832 analysis of debris-flow flexible barrier capacity from momentum and energy
833 perspectives. Eng. Geol. 251, 81-92.
834 Suda, J., Strauss, A., Rudolf-Miklau, F., Hübl, J., 2009. Safety assessment of barrier
835 structures. Struct. Infrastruct. Eng. 5 (4), 311-324.
836 Suda, J., Hübl, J., Bergmeister, K., 2010. Design and construction of high stressed
837 concrete structures as protection works for torrent control in the Austrian Alps. In
838 Proc. of the 3rd fib international Congress, Washington, USA.

VanDine, D.F., 1996. Debris flow control structures for forest engineering. Research Branch, BC Ministry of Forests, Victoria, BC. Working paper 08/1996. 75 pages.

Volkwein, A., 2014. Flexible Debris Flow Barriers: Design and Application, Swiss Federal Institute for Forest, Snow and Landscape Research, WSL Berichte 18, p. 32.

Watanabe M., Ikeya H., 1981. Investigation and analysis of volcanic mud flows on Mount Sakurajima Japan. In Erosion Sediment Transport Measurement (Proceedings of the Florence Symposium, June 1981), 245-256.

WLV, 2006. Jahresbericht 2005 des Forsttechnischen Dienst für Wildbach-und Lawinenverbauung [Annual Report 2005 of Section Forestry in the the Austrian service for Torrent and Avalanche Control].Wien: Bundesministerium für Land-und Forstwirtschaft, Umwelt und Wasserwirtschaft, Sektion Forst, Wildbach-und Lawinenverbauung.

Wei, Z.L., Shang, Y.Q., Lü, Q., Yu, Z., Pan, P., 2017. Application and design of an efficient siphon dewatering system for debris flow mitigation: a case study of a small catchment in Zhejiang Province, China. Eng. Geol. 226, 146-160.

Wendeler, C., Volkwein, A., Roth, A., Denk, M., & Wartmann, S., 2007. Field measurements and numerical modelling of flexible debris flow barriers. Debris-Flow Hazards Mitig. Mech. Predict. Assess. Millpress, Rotterdam, 681-687.

Xie, T., Wei, F., Yang, H., Gardner, J.S., Xie, X., 2017. A design method for a debris flow water-sediment separation structure. Eng. Geol. 220, 94-98.

Yan, S., He, S., Deng, Y., Liu, W., Wang, D., Shen, F., 2020. A reliability-based approach for the impact vulnerability assessment of bridge piers subjected to debris flows. Eng. Geol. 105567.

Zhang, S., 1993. A comprehensive approach to the observation and prevention of debris flows in China. Nat. Hazards 7 (1), 1-23.

Zhou, G.G.D., Ng, C.W.W., 2010. Dimensional analysis of natural debris flows. Can. Geotech. J. 47 (7), 719-729.

Zhou, G.G.D., Hu, H.S., Song, D., Zhao, T., Chen, X.Q., 2019a. Experimental study on the regulation function of slit dam against debris flows. Landslides 16 (1), 75-90.

Zhou, G.G.D., Li, S., Song, D., Choi, C.E., Chen, X.Q., 2019b. Depositional mechanisms and morphology of debris flow: physical modelling. Landslides 16 (2), 315-332.

Zhou, G.G.D., Du, J., Song, D., Choi, C.E., Hu, H.S., Jiang, C., 2020. Numerical study of granular debris flow run-up against slit dams by discrete element method. Landslides 17(3): 585–595.

List of figures

Fig. 10 (a) Empirical dynamic pressure coefficient (α_1) deduced from the maximum frontal impact pressure (P_{peak}) and **(b)** empirical dynamic pressure coefficient (α_2) deduced from the peak impact force (F_{peak}) exerted on the dams with unit width at different relative slit size (b/D_{max}).

Fig. 11 (**a)** Relationship between the deduced empirical dynamic pressure coefficients (α_1) and Froude number (Fr); **(b)** the values of Savege number (N_{sav}) for the tests with C_s=0.4 and C_s=0.6.

Fig. 12 Time series of the degree of liquefaction (u_w/σ) in the series of tests **(a)** 15-0.4 and **(b)** 15-0.6. In both series of tests, the size of the dams are varied from 4.5 to 0 (check dam).

Fig. 13 Impact pressure profiles when peak pressures, peak forces, and until static conditions were measured for tests **(a)** C15-0.4-0 (check dam); **(b)** S15-0.4-1.8; **(c)** S15-0.4-3.6; **(d)** C15-0.6-0 (check dam); **(e)** S15-0.6-1.8; and **(f)** S15-0.6-3.6. H_i (i=1,2,3,4,5) is the height of impact force sensors on model dams; h is the flow depth.

Fig. 14 Comparison of the impact pressure distribution models on countermeasure structures. The structure height (H), flow depth (h), and the peak impact pressure (P_{peak}) denoted in the diagrams. (a) the conventional pressure distribution models for closed-type dam (e.g., check dam) include the triangle model (a_1), trapezoid model (a_2) and rectangle model (a_3); (b) the revised triangular pressure distribution model for closed-type dam from Song et al. (2017); (c) the impact pressure distribution models for the open-type dam (e.g., slit dam), (c_1) the double rectangular distribution model for the granular debris flow impact and (c_2) the bilinear trapezoidal distribution model for the muddy debris flow impact; (d) the inverse trapezoid (higher pressure at free surface) pressure distribution model reported by Cui et al. (2015); the new bilinear triangular pressure distribution model proposed in this study, (e_1) for check dam and slit dam with $b/D_{max}\leq1.8$, and (e_2) for the slit dam with $b/D_{max}>1.8$.

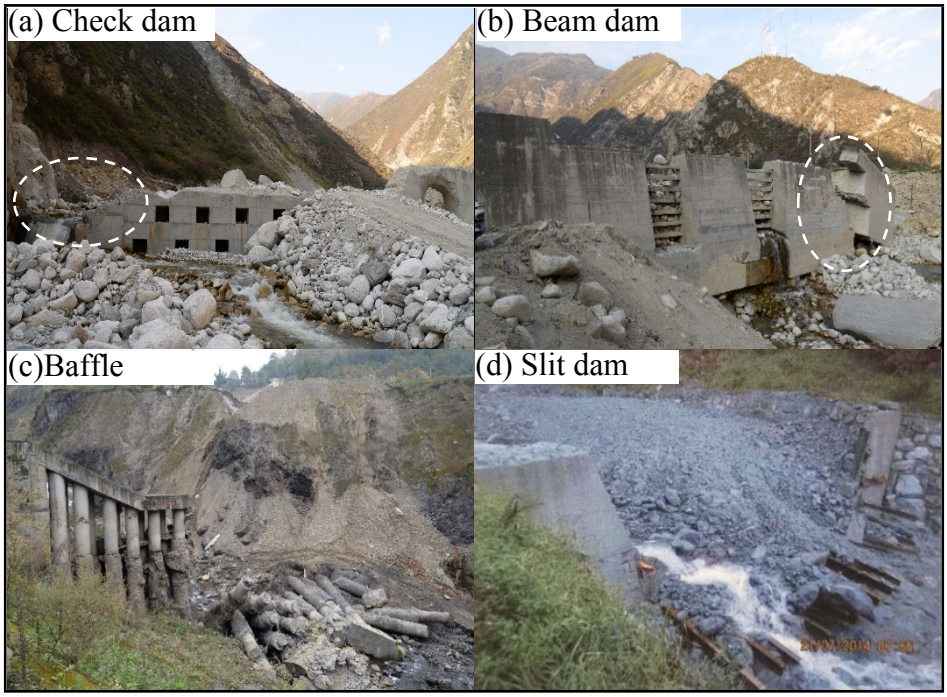

Fig. 1 Failure cases of structural countermeasures for debris flow mitigation: **(a)** concrete check dam; **(b)** concrete beam dam constructed in Wenchuan city, Sichuan province, China; **(c)** a baffle constructed in Beichuan city, Sichuan province, China (the photograph taken in 2019); and **(d)** a steel slit dam in Schwaighofgraben, Salzburg, destroyed by debris flows (courtesy of Leonardi et al., 2019a).

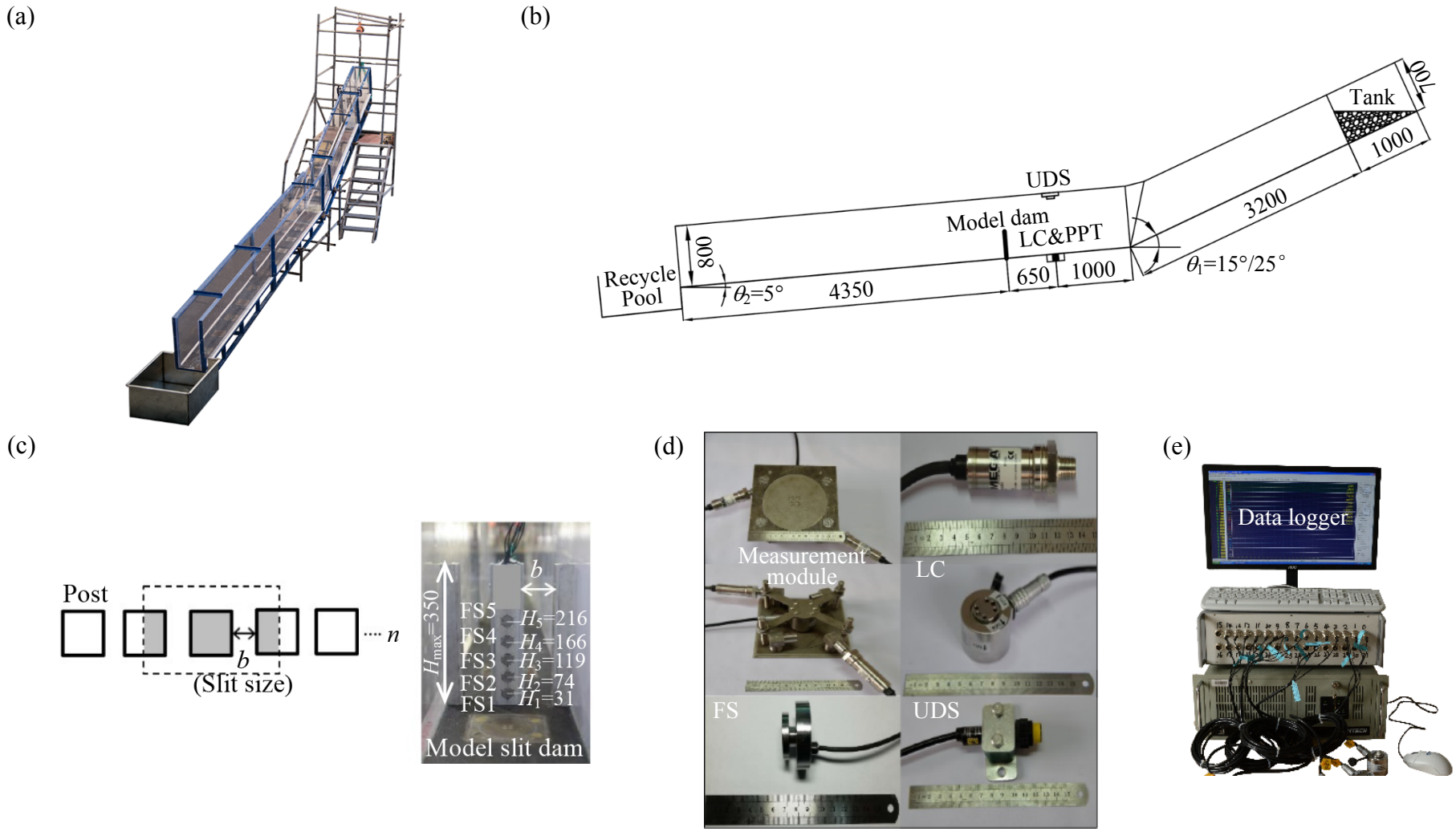

Fig. 2 Setup and instrumentation of flume model tests (all dimensions in mm). **(a)** the photograph of model flume; **(b)** the side view schematic of the model flume, the high-speed camera set to 250 fps; **(c)** model slit dam, the FS1-FS5 represents the number of impact force sensor; H_1-H_5 represents the height of sensors on slit dam; H_{max} is the height of model dam; **(d)** instrumentation, including the measurement module consist of the pore water pressure sensor (PPT) and the load cell (LC) used to measure the pore water pressure and normal stress of debris flow, respectively; the impact force sensor (FS), , and the ultrasonic distance sensor (UDS); and **(e)** data logger, the frequency set to 500Hz.

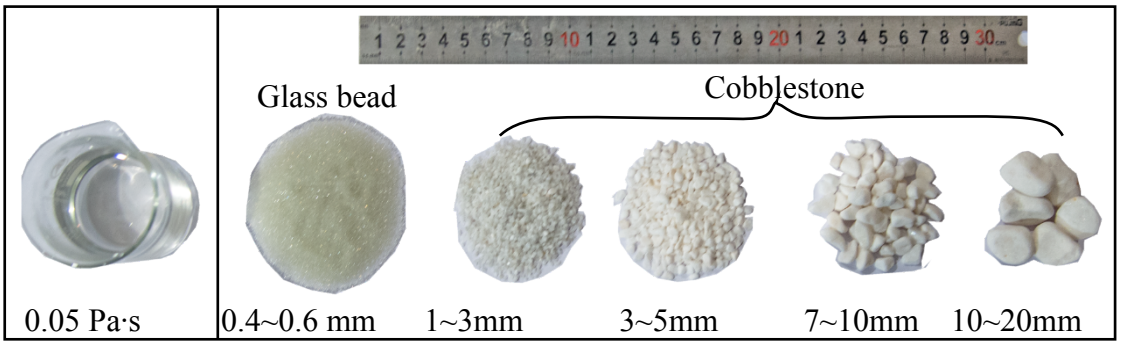

Fig. 3 Materials used in the tests. The mixture of glycerol and water used as liquid phase, the glass bead and cobblestone used to model granular material of debris flow.

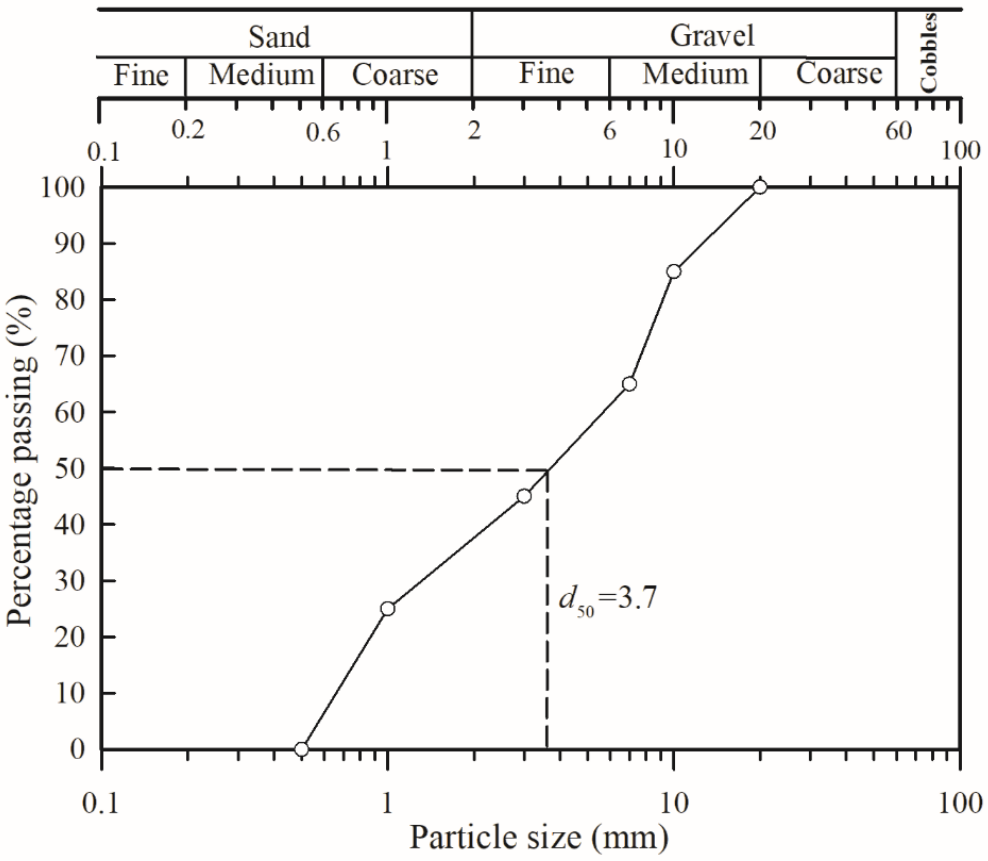

Fig. 4 Particle size distribution of the granular material.

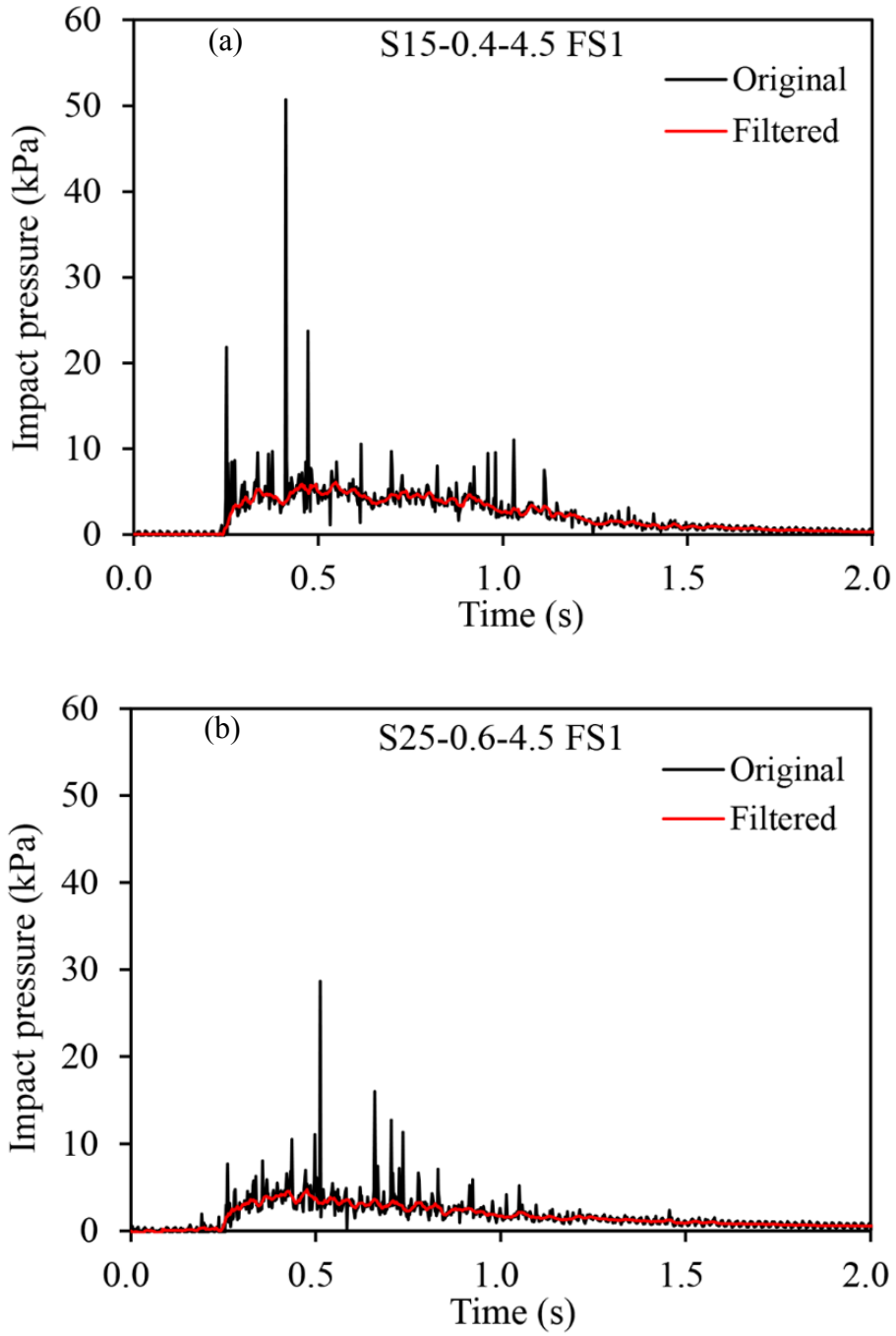

Fig. 5 Time series of filtered impact pressure caused by continuous hydraulic impact (read solid line) recorded by the impact force sensor "FS1" in test S15-0.4-4.5 (a) and S25-0.6-4.5 (b). The black solid line represents the original impact pressure in the tests.

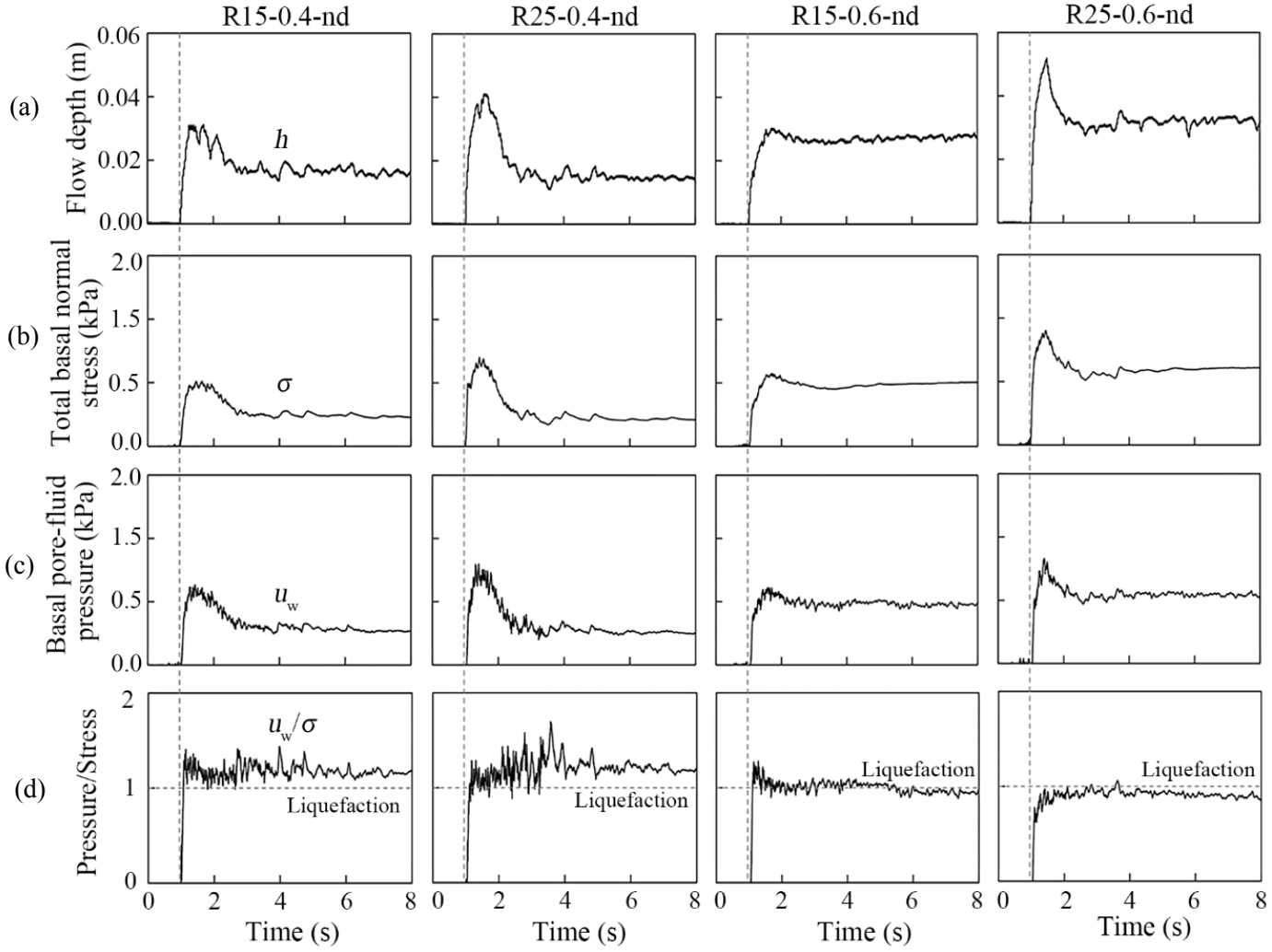

Fig. 6 Measurements of **(a)** flow depth, **(b)** total basal normal stress, and **(c)** basal pore-fluid pressure of the flow front made at 0.65 meters upstream the slit dam for the reference tests with different flume inclination (θ_1=15° and 25°) and with different solid fraction (C_s=0.4 and 0.6): test R15-0.4-nd, R25-0.4-nd, R15-0.6-nd and R25-0.6-nd. **(d)** The ratio of the basal pore-fluid pressure to the basal normal stress.

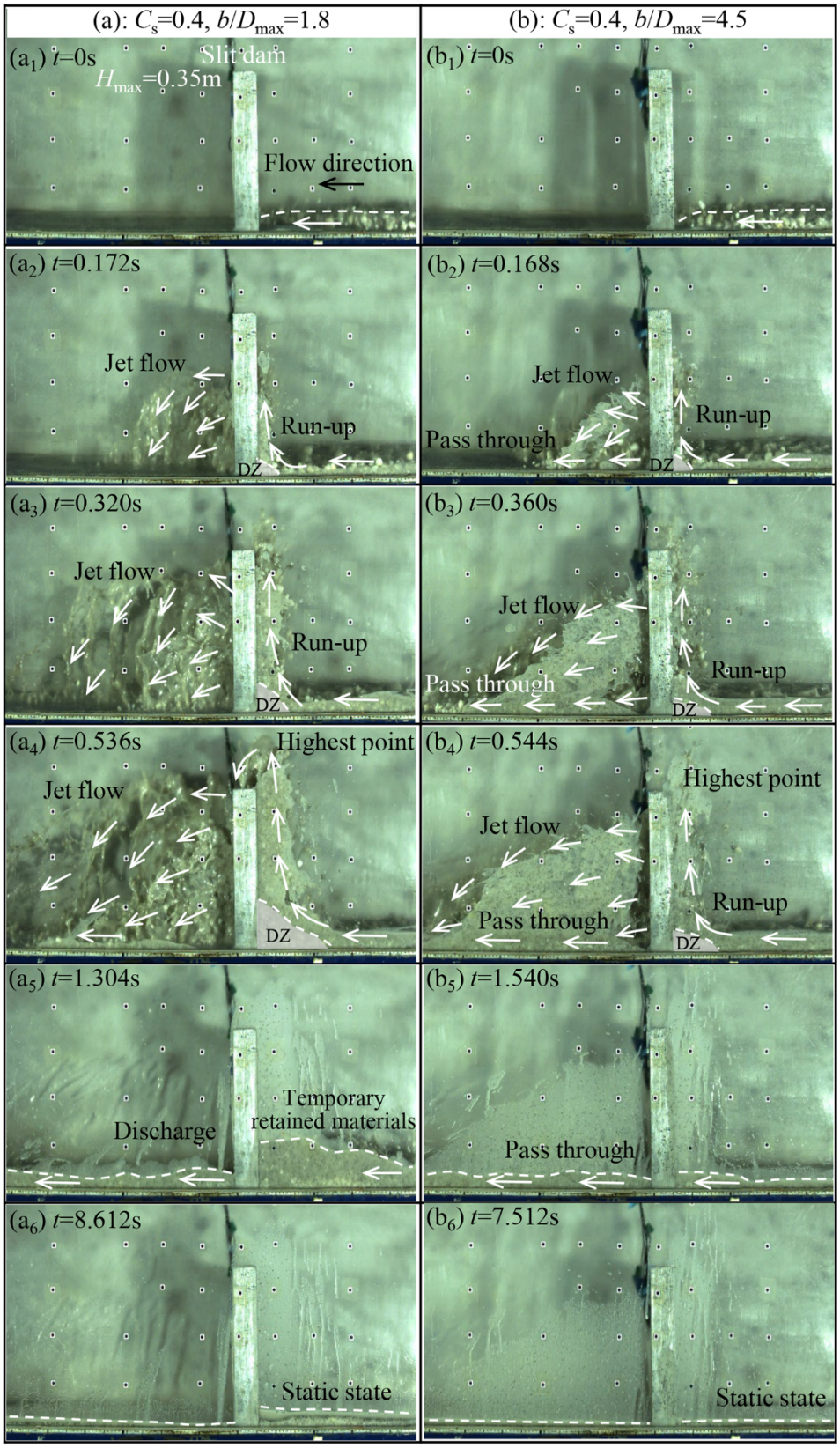

Fig. 7 Impact process of debris flow with solid fraction C_s**=0.4** against slit dam with narrow (b/D_{max}=1.8) and wide (b/D_{max}=4.5) relative slit size when the channel inclination is 15°, i.e., the test S15-0.4-1.8 and test S15-0.4-4.5; DZ represents "dead zone" shown in the gray area.

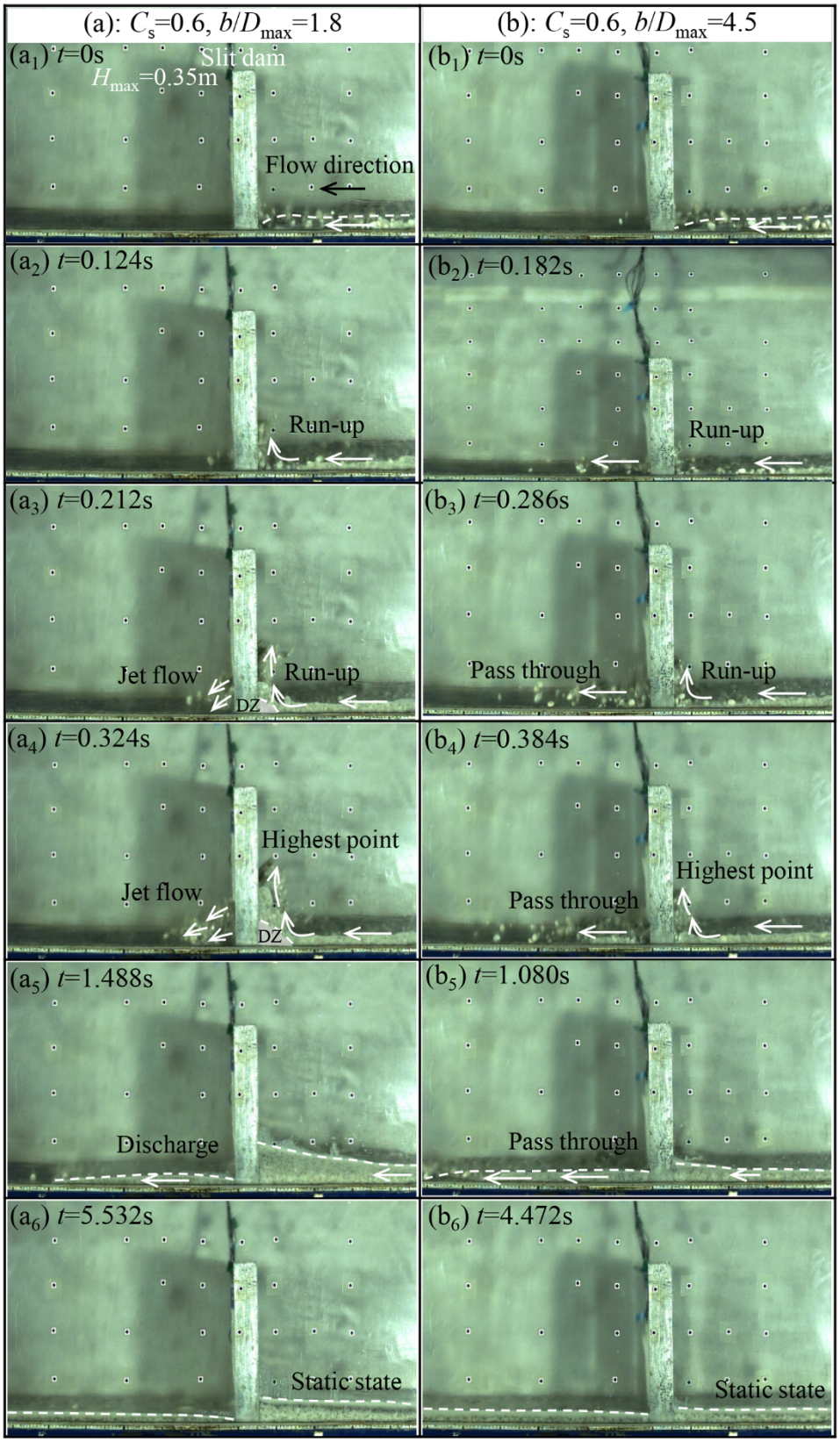

Fig. 8 Impact process of debris flow with solid fraction C_s**=0.6** against slit dam with narrow (b/D_{max}=1.8) and wide (b/D_{max}=4.5) relative slit size when the channel inclination is 15°: test S15-0.6-1.8 and test S15-0.6-4.5; DZ represents "dead zone" shown in the gray area.

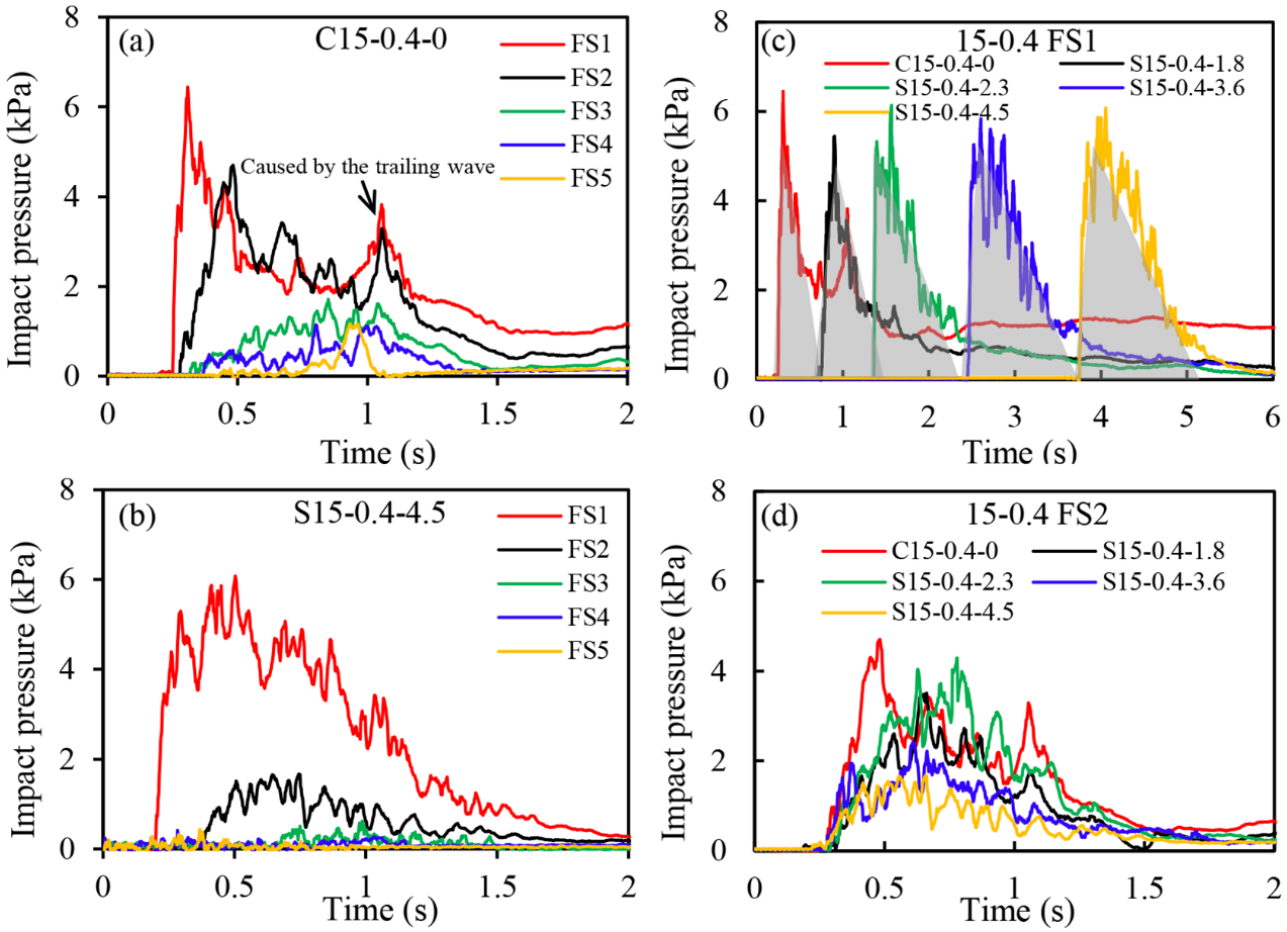

Fig. 9 Time series of the impact pressure of tests **(a)** C15-0.4-0 (check dam) and **(b)** S15-0.4-4.5. Comparison of the impact pressures detected by **(c)** FS1 and **(d)** FS2 in the tests with channel inclination θ_1=15° and solid fraction C_s=0.4. Relative slit size b/D_{max} is varied from 0 to 4.5.

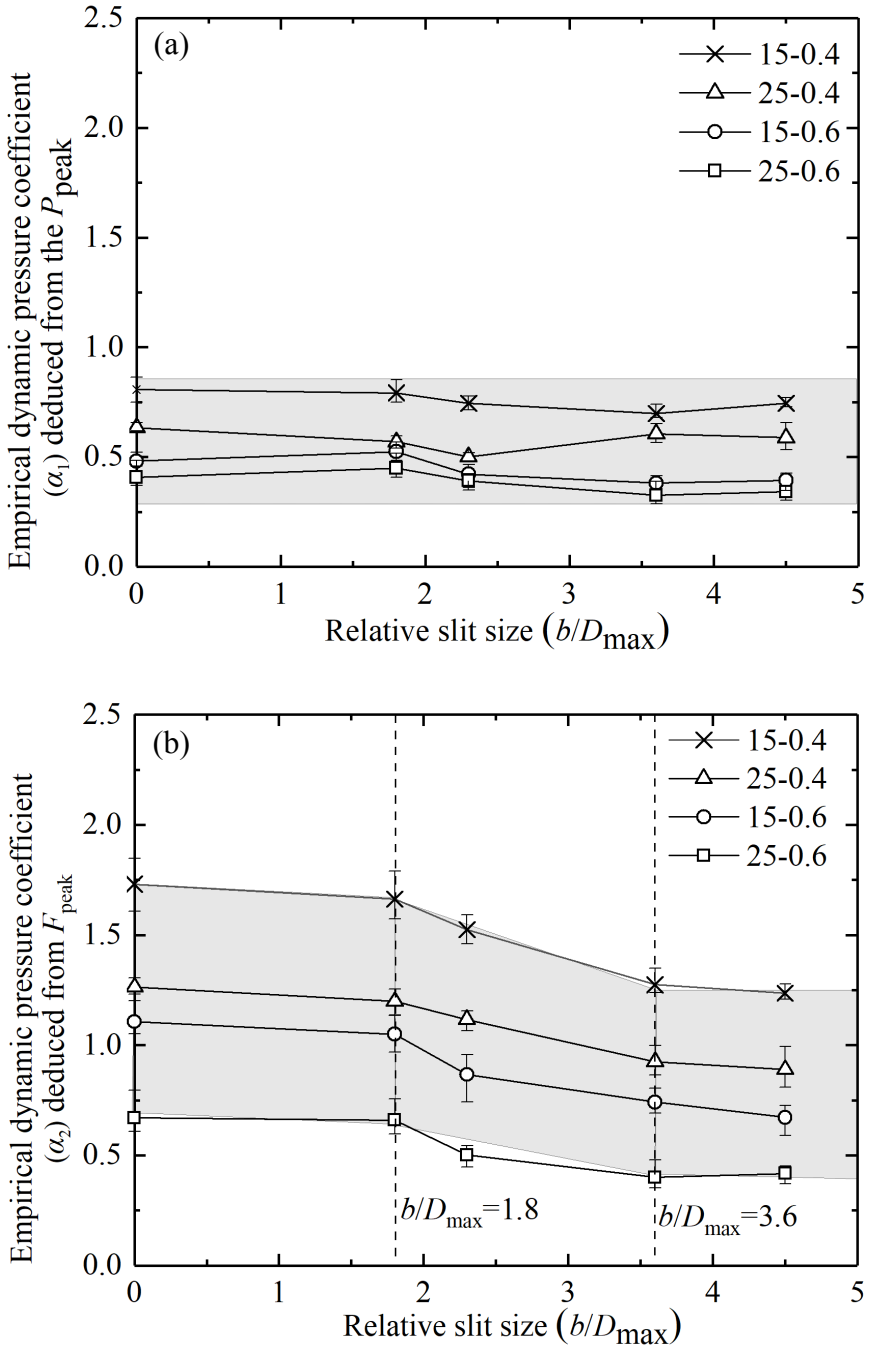

Fig. 10 (a) Empirical dynamic pressure coefficient (α_1) deduced from the maximum frontal impact pressure (P_{peak}) and **(b)** empirical dynamic pressure coefficient (α_2) deduced from the peak impact force (F_{peak}) exerted on the dams with unit width at different relative slit size (b/D_{max}).

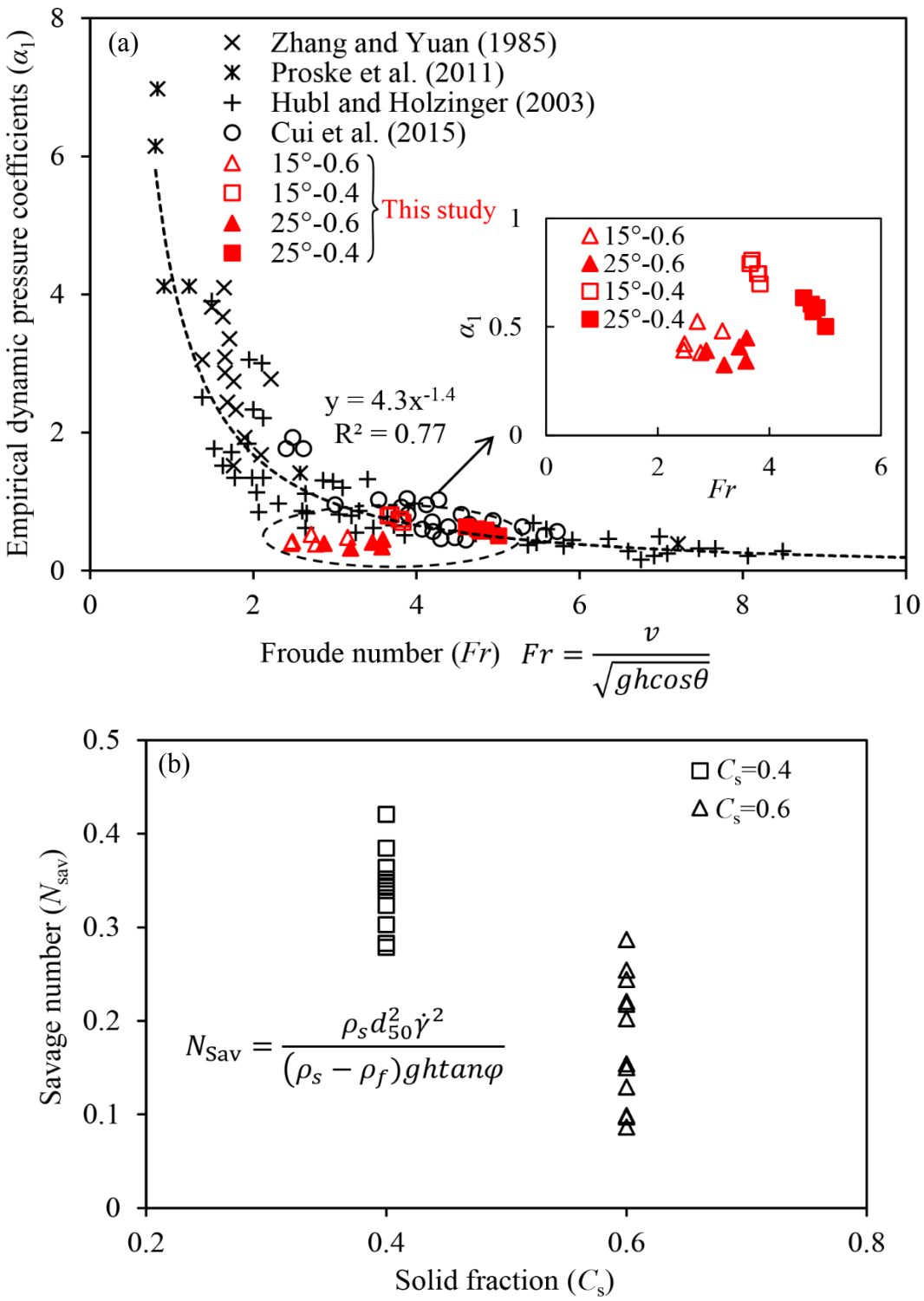

Fig.11 (a) Relationship between the deduced empirical dynamic pressure coefficients (α_1) and Froude number (Fr); **(b)** the values of Savege number (N_{sav}) for the tests with C_s=0.4 and C_s=0.6.

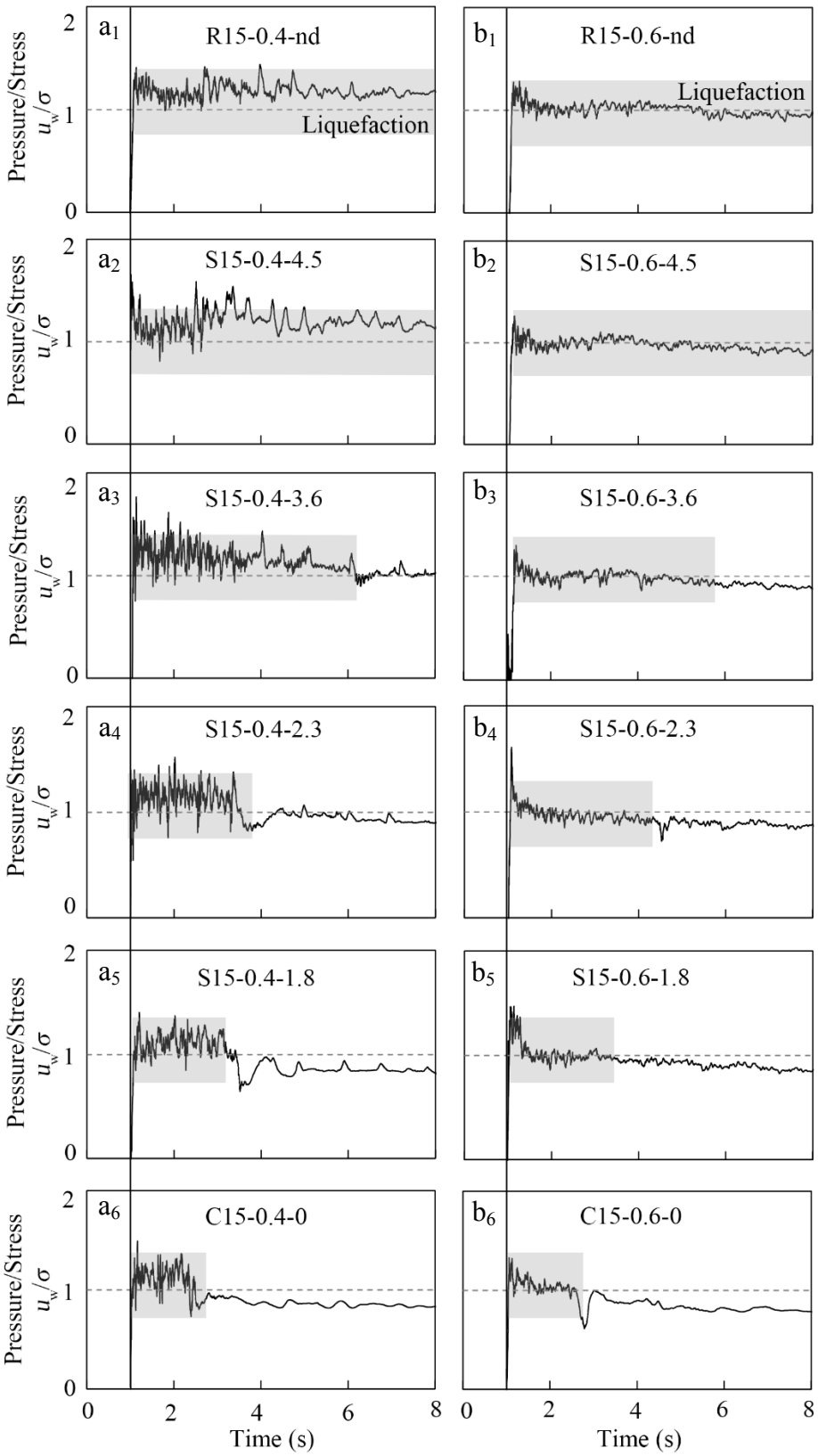

Fig. 12 Time series of the degree of liquefaction (u_w/σ) in the series of tests **(a)** 15-0.4 and **(b)** 15-0.6. In both series of tests, the relative slit size of the dams varied from 4.5 to 0 (check dam)

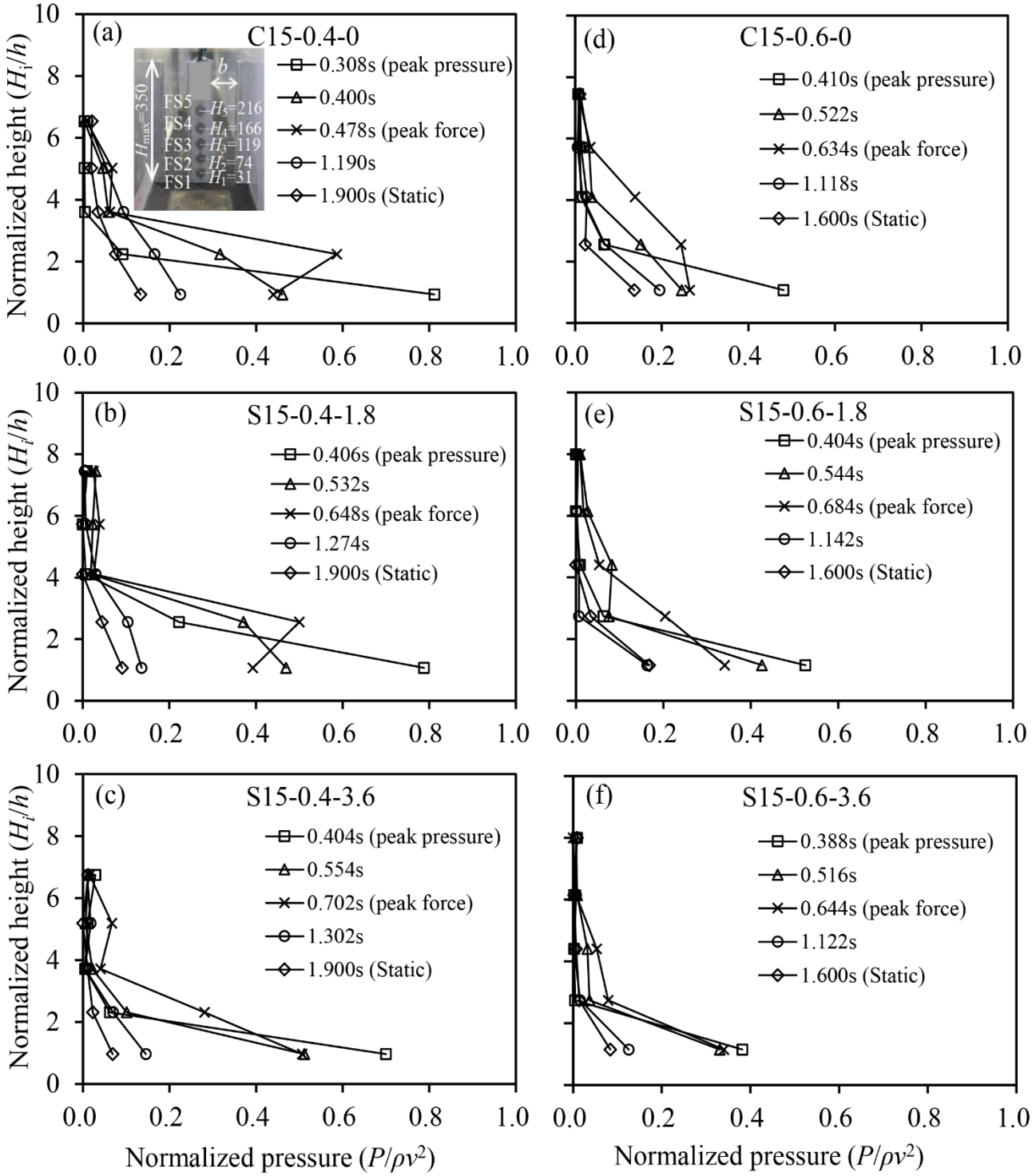

Fig. 13 Impact pressure profiles when peak pressures, peak forces, and until static conditions were measured for tests **(a)** C15-0.4-0 (check dam); **(b)** S15-0.4-1.8; **(c)** S15-0.4-3.6; **(d)** C15-0.6-0 (check dam); **(e)** S15-0.6-1.8; and **(f)** S15-0.6-3.6. H_i (i=1,2,3,4,5) is the height of impact force sensors on model dams; h is the flow depth.

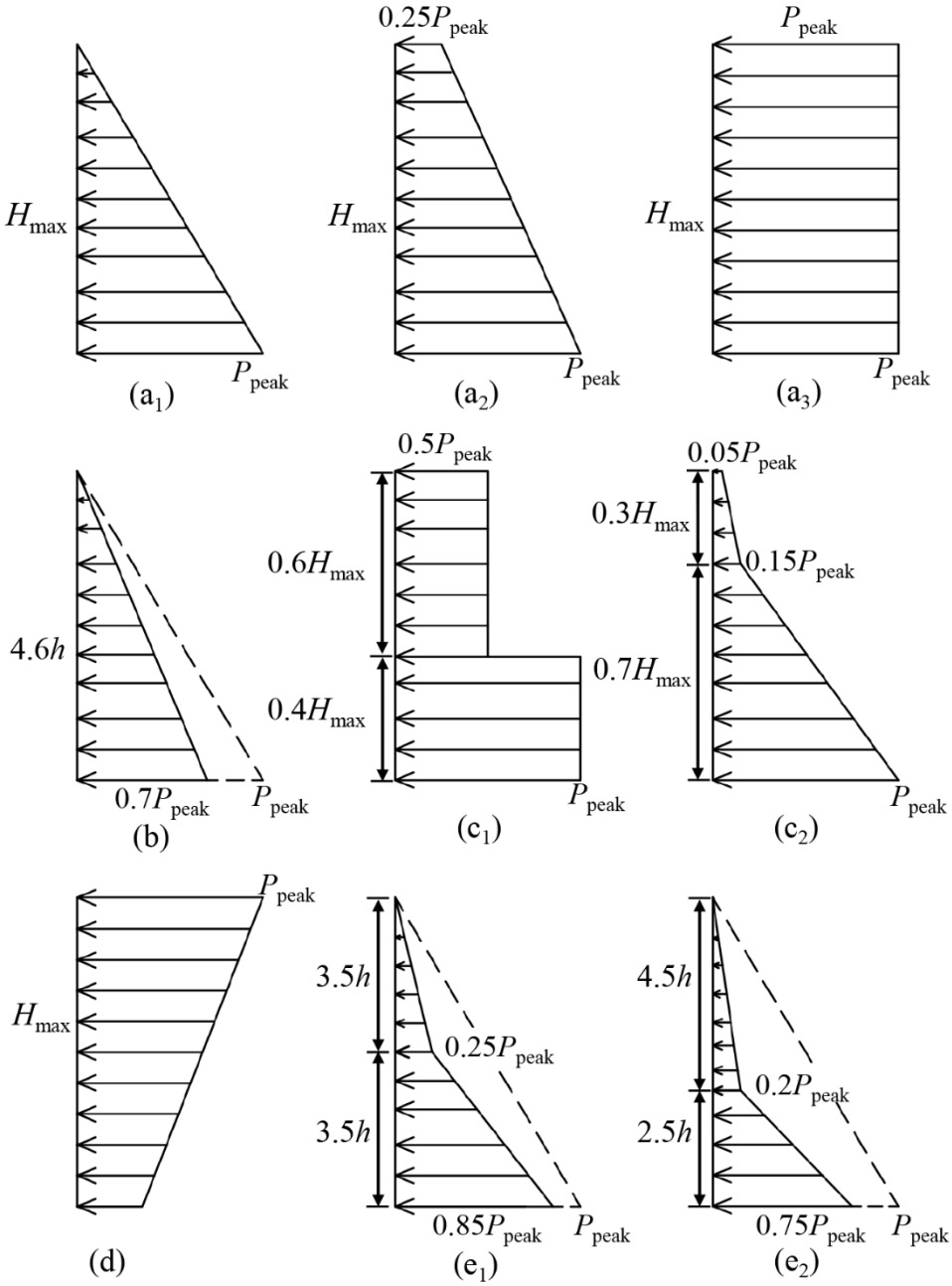

Fig. 14 Comparison of the impact pressure distribution models on countermeasure structures. The structure height (H), flow depth (h), and the peak impact pressure (P_{peak}) denoted in the diagrams. (a) the conventional pressure distribution models for closed-type dam (e.g., check dam) include the triangle model (a_1), trapezoid model (a_2) and rectangle model (a_3); (b) the revised triangular pressure distribution model for closed-type dam from Song et al. (2017); (c) the impact pressure distribution models for the open-type dam (e.g., slit dam), (c_1) the double rectangular distribution model for the granular debris flow impact and (c_2) the bilinear trapezoidal distribution model for the muddy debris flow impact; (d) the inverse trapezoid (higher pressure at free surface) pressure distribution model reported by Cui et al. (2015); the new bilinear triangular pressure distribution model proposed in this study, (e_1) for check dam and slit dam with $b/D_{max} \leq 1.8$, and (e_2) for the slit dam with $b/D_{max} > 1.8$.

Table 1 Summary of hydro-dynamic models for estimating debris flow impact pressure

Pressure coefficient ($\alpha=P/\rho v^2$)	**Remarks**			**Reference**	**Data source**
	Structure type	Flow type	Froude number (Fr)		
α=0.4~1.2	Rigid barrier	Dry sands;	4.1~5.9	Ng et al. (2016)	Small-scale experiments
α=1.4~1.6	Rigid barrier	Viscous fluids;	3.2~3.9		
α=0.4~2.0	Column	Viscous debris flow, Coarse particles removed;	2.5~5.9	Cui et al. (2015)	
α=0.1~3.9	Slit dam	Flow with coarse and flow with fine particles;	1.2~13.0	Hübl and Holzinger (2003)	
α=1.5~5.5	Rigid barrier; flexible barrier	Fine sand flow with solid volume fraction equal to 0.6;	/	Canelli et al. (2012)	
α=0.2~1.0	Column	Viscous debris flow in Jiangjia Ravine, China. Coarse particles removed;	1.5~3.0	Hu et al. (2011)	Field measurements
α=1.5	/	Back analysis of the stony-debris flow in British Columbia, Canada;	/	Hungr et al. (1984)	
α=2.0	/	Volcanic debris flow with boulders;	/	Watanabe and Ikeya (1981)	
α=3~5	Column	Viscous debris flow in Jiangjia Ravine, China. Coarse particles not removed;	/	Zhang (1993)	
α=1.0	Circular structure	Flows without big boulders;	/		Guidances for mitigation design
α=1.33	Rectangular structure	Flows without big boulders;	/	MLR (2004)	
α=1.47	Square structure	Flows without big boulders;	/		
α=1.0	/	/	/	NILIM (2007)	
α=2.5~3	/	To estimate the dynamic debris impact pressure in combination with boulder impact load.	/	GEO Report No.104 (Lo, 2000); GEO Report No.207 (Kwan 2012)	

Table 2 Comparison of the dimensionless numbers that characterize stresses between in the range of prototypical debris flows and physical experiments

Debris flow types	Dimensionless numbers			Reference
	Bagnold number (N_{Bag})	**Savage number (N_{Sav})**	**Friction number (N_{Fric})**	
Oddstad Debris Flow Jan. 4, 1982	4	2×10^{-4}	2×10^{4}	Iverson, 1997a
South Toutle River, May 18,1980	0.2	6×10^{-6}	3×10^{4}	
Osceola Mudflow, circa 5700 B.P.	0.4	1×10^{-7}	4×10^{6}	
Kamikamihorizawa Debris Flow	1×10^{4}	3×10^{-2}	3×10^{5}	
Mount St. Helens pyroclastic flows	9×10^{5}	4×10^{-3}	2×10^{8}	Iverson and Vallance, 2001
Elm Rock avalanche	4×10^{8}	0.1	4×10^{9}	
Typical range of natural debris flows	**$1\sim10^{8}$**	**$10^{-7}\sim1$**	**$1\sim10^{5}$**	**Haas et al., 2015**
USGS flume experiments	400	0.20	2×10^{3}	Iverson, 1997a
Small-scale flume experiments	37~1589	0.17~2.25	141~2760	Haas et al., 2015
	45~314	0.5~9.0	25~64	Zhou et al., 2019b
	8×10^{4}	0.1	8×10^{5}	Iverson and Vallance, 2001
	31.8~65.4	**0.09~0.42**	**87.5~534.0**	**This study**

Table 3 Test program of debris flow-slit dam interaction

Test ID	Relative slit size b/D_{max}	Slope θ_1 (°)	Bulk density (kg/m³)	Solid fraction (C_s)	Approach velocity （m/s）	Flow depth (m)	Froude number Fr	Bagnold number N_{Bag}	Savage number N_{Sav}	Friction number N_{Fric}
R15-0.4-nd	No dam	15	1819	0.4	2.06	0.031	3.73	33.2	0.35	94.6
C15-0.4-0	Check dam				2.09	0.033	3.69	31.8	0.30	105.2
S15-0.4-1.8	1.8				1.95	0.029	3.65	33.6	0.38	87.5
S15-0.4-2.3	2.3				2.13	0.032	3.81	33.3	0.34	97.4
S15-0.4-3.6	3.6				2.14	0.032	3.83	33.6	0.35	96.7
S15-0.4-4.5	4.5				2.12	0.032	3.79	33.2	0.34	97.8
R25-0.4-nd	No dam	25	1819	0.4	3.09	0.041	4.89	37.8	0.34	110.0
C25-0.4-0	Check dam				2.99	0.043	4.61	34.9	0.28	125.1
S25-0.4-1.8	1.8				2.95	0.039	4.78	38.0	0.36	104.3
S25-0.4-2.3	2.3				3.05	0.038	5.01	40.3	0.42	95.7
S25-0.4-3.6	3.6				3.12	0.044	4.75	35.5	0.28	125.7
S25-0.4-4.5	4.5				3.11	0.042	4.85	37.1	0.32	114.8
R15-0.6-nd	No dam	15	2128	0.6	1.46	0.029	2.75	57.0	0.22	261.6
C15-0.6-0	Check dam				1.68	0.029	3.16	65.4	0.29	227.8
S15-0.6-1.8	1.8				1.39	0.027	2.71	58.2	0.24	238.4
S15-0.6-2.3	2.3				1.25	0.026	2.48	54.3	0.22	246.1
S15-0.6-3.6	3.6				1.42	0.027	2.77	59.4	0.25	233.6
S15-0.6-4.5	4.5				1.27	0.027	2.47	52.9	0.20	262.0
R25-0.6-nd	No dam	25	2128	0.6	2.22	0.050	3.17	50.0	0.10	513.8
C25-0.6-0	Check dam				2.27	0.044	3.46	58.2	0.15	388.4
S25-0.6-1.8	1.8				2.38	0.045	3.59	59.7	0.15	387.3
S25-0.6-2.3	2.3				1.96	0.048	2.87	46.2	0.09	534.0
S25-0.6-3.6	3.6				2.23	0.050	3.19	50.4	0.10	510.1
S25-0.6-4.5	4.5				2.48	0.049	3.58	57.0	0.13	441.3

Declaration of interests

- The authors declare that they have no known competing financial interests or personal relationships that could have appeared to influence the work reported in this paper.

- The authors declare the following financial interests/personal relationships which may be considered as potential competing interests:

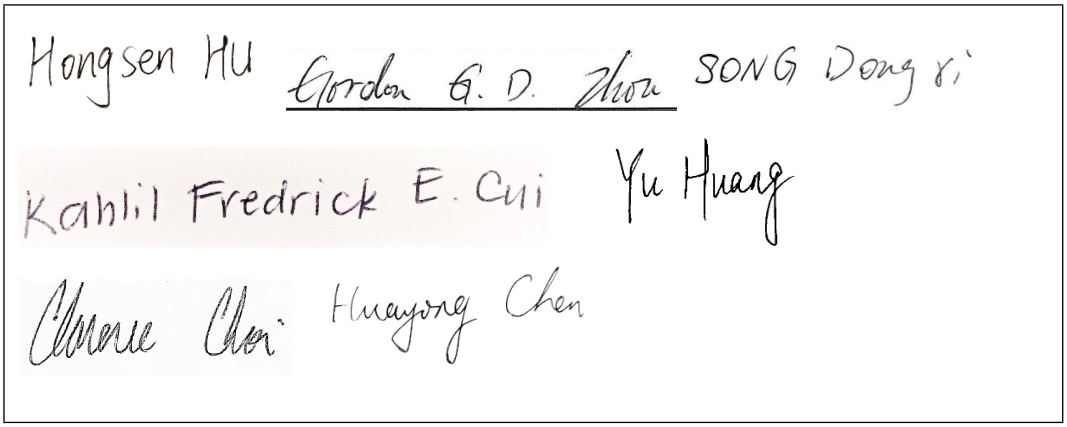

Author Statement

Hongsen Hu: Conceptualization, Methodology, Writing-Original draft preparation. **Gordon G. D. Zhou**: Conceptualization, Writing-Reviewing & Editing. **Dongri Song**: Conceptualization, Writing- Reviewing & Editing. **Kahlil Fredrick E. Cui**: Methodology, Writing-Reviewing & Editing. **Yu Huang**: Writing-Reviewing & Editing. **Clarence E. Choi**: Methodology, Writing-Reviewing & Editing. **Huayong Chen**: Writing- Reviewing & Editing.